LINKED-CLUSTER EXPANSIONS OF PERTURBED TOPOLOGICAL PHASES

Masters's Thesis in Physics

Presented by

Viktor Kott

31.10.2022

Institute for Theoretical Physics I
Friedrich-Alexander-Universität Erlangen-Nürnberg

Supervisor: Prof. Dr. Kai Philipp Schmidt

Abstract

We investigate the robustness of Kitaev's toric code in a uniform magnetic field on the square and honeycomb lattice by perturbative linked cluster expansions using a full graph decomposition. In particular, the full graph decomposition allows to correctly take into account the non-trivial mutual exchange statistics of the elementary anyonic excitations. This allows us to calculate the ground-state energy and excitation energies of the topological phase which are then used to study the quantum phase transitions out of the topologically ordered phase as a function of the field direction.

Contents

1. Introduction

While the existence of topological order was already proposed in 1989 by Wen et al. to characterize the ground state of high-temperature superconductors [1–3], it is still object to much research and was studied for many different spin models during the last decades [4–10]. The topological phases, which correspond to a topological order, are characterized by the presence of anyons, which are particles only occuring in two dimensions, and nontrivial ground states [8]. These ground states are highly non-local. Calculating phase transitions proves to be a problem for the conventional method of Landau's symmetry breaking theory, since it uses local quantities. Hence, topologically ordered systems have to be characterized by global operators.

A prominent model with intrinsic topological order is the two-dimensional toric code, which was introduced and solved by Kitaev [5]. While the toric code itself is hard to realize experimentally, the ground state of the toric code has been prepared on a superconducting quantum processor [11]. The toric code was also used for quantum simulations of anyons [12].

In this thesis, we will perturb the topological phase of the toric code and investigate the phase transitions. Although topological ordered phases are known to be stable under local perturbations, proven in [13], this is no longer true for strong, global perturbations. Various perturbations, e.g. thermal [14] and magnetic perturbations [15–21] and noise [22] have already been considered. The toric code has also been studied under magnetic perturbation and geometric frustration [23]. In our case, we will analyze the toric code in the thermodynamic limit at zero temperature. In this case, the simplest form of perturbation is a magnetic field. Since we consider an infinite system with highly non-local ground states, where the non-locality does not allow local order parameters, it seems counter-intuitive to analyze the toric code on finite subsystems. Nonetheless, a finite-lattice method [24] has been used successfully to probe the robustness of the toric code in an uniform field [21, 25]. In this thesis, we will use a similar approach, namely the linked-cluster expansion. Our method differs from the finite-lattice method, since we apply perturbation theory on calculated graphs, instead of the clusters directly. This allows us, to calculate physical quantities on finite clusters and not the infinite system, but still obtain results in the thermodynamic limit after proper embedding.

In this work, we will consider the toric code on a square and honeycomb lattice. The models will be introduced in chapter 2. Here the basic properties and effects of a

magnetic field will be discussed.

With perturbative continuous unitary transformations [26, 27] and linked-cluster expansions [28, 29], which are described in chapter 3, we will calculate relevant quantities of the toric code for different field directions and present them in chapter 4. There, our results for the square lattice are compared to [21]. We will further consider the toric code on a honeycomb lattice. This model was not the object of any quantitative study yet. Here we will mirror considerations done for the model on the square lattice and present a quantum phase diagram for the uniform magnetic field.

2. The toric code in a field

In the following chapter we introduce the toric code on a square lattice and its exact solution [5]. The behaviour and statistics of elementary excitations are investigated. We then introduce a magnetic field and analyze the limiting cases, that suggest a quantum phase transition. Lastly, we introduce the toric code on a honeycomb lattice and identify key differences.

2.1   The toric code on a square lattice

We begin this section by introducing the toric code. Here we will examine the ground-state properties and find that the system exhibits a intrinsic topological order. Next, we study the elementary excitations, which show non-trivial exchange statistics and, for finite magnetic fields, become dispersive. This can be used to calculate critical points, as it will be shown in section 4.1. For certain field configurations, exact mappings on to known models can be found and will be discussed.
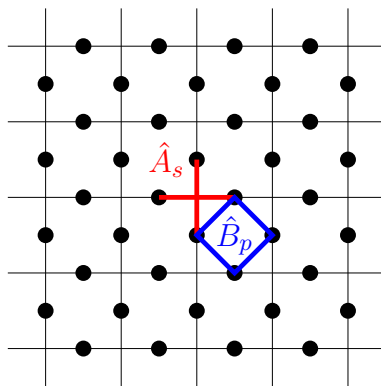

Figure 2.1: Square lattice with plaquettes p (blue) and stars s (red) and the operators $\hat{B}_p$ and $\hat{A}_s$ acting on plaquettes and stars respectively.

2.1.1 Properties of the toric code on a square lattice

The conventional toric code [5] is a spin model, defined on a two-dimensional lattice. Extensions to three dimensions are possible and have been studied in [30]. In this thesis, we investigated the toric code on a on a square lattice, as seen in Figure 2.1, which is already well known [18, 19]. Here the Hamiltonian reads:

$$\hat{H}_{\mathrm{TC}} = -J_s \sum_s \hat{A}_s - J_p \sum_p \hat{B}_p. \tag{2.1}$$

$$\hat{A}_s = \prod_{i \in s} \sigma_i^x \tag{2.2}$$

$$\hat{B}_p = \prod_{i \in p} \sigma_i^z \tag{2.3}$$

The star and plaquette operators $\hat{A}_s$ and $\hat{B}_p$, which are products of Pauli matrices σ^α, are acting on the four spins contained in stars or plaquettes. Since all stars and plaquettes always share an even number of spins, the operators $\hat{A}_s$ and $\hat{B}_p$ commute. It follows, that $\hat{A}_s$ and $\hat{B}_p$ also commute with $\hat{H}_{\mathrm{TC}}$, hence their eigenvalues are conserved quantities. Additionally, one can easily see that $\hat{A}_s^2 = \hat{B}_p^2 = \mathbb{1}$, which fixes the eigenvalues a_s and b_p to be ± 1. For $J_s, J_p > 0$ the ground state of the toric code can be constructed by setting the eigenvalues a_s and b_p to $+1$. The ground state on the open plane can be written as:

$$|0\rangle = \mathcal{N} \prod_s (1 + \hat{A}_s) \prod_p (1 + \hat{B}_p) |\Rightarrow\rangle = \mathcal{N}_p \prod_p (1 + \hat{B}_p) |\Rightarrow\rangle. \tag{2.4}$$

This ground state is unique, since for other topologies than the open plane, new, topological properties arise, which will be discussed in the next subsection. In Equation 2.4, the reference state $|\Rightarrow\rangle = |\rightarrow\rightarrow \cdots \rightarrow\rangle$ with $\sigma^x |\rightarrow\rangle = +1 |\rightarrow\rangle$ was chosen. Acting with σ_i^z on the reference state flips the spin on site i, such that $\sigma_i^z |\rightarrow ... \rightarrow\rangle = |\rightarrow ... \rightarrow\leftarrow\rightarrow ... \rightarrow\rangle$. While choosing other suitable reference states would yield the same result, some reference states are preferable, like discussed in subsection 3.2.3. The operator sequence $\mathcal{N} \prod_s (1 + \hat{A}_s) \prod_p (1 + \hat{B}_p)$ projects the reference state onto a subspace of states, in which every $\hat{A}_s$ and $\hat{B}_p$ takes the value $+1$. The normalisation constant $\mathcal{N}$ is determined by the number of terms in the sum given by $\prod_p (1 + \hat{B}_p)$. For N_p plaquettes and N_s stars, the sum consists of 2^{N_s} and 2^{N_p} terms which allows us to identify $\mathcal{N} = \frac{1}{\sqrt{2^{N_p} 2^{N_s}}}$. On the square lattice the number of stars and plaquettes are the same, such that $\mathcal{N} = \frac{1}{2^N}$. It follows, that $\mathcal{N}_p = \mathcal{N} 2^{N_s}$.

To gain further understanding of the ground state $|0\rangle$, one can take a closer look at the projector $\prod_p (1 + \hat{B}_p)$:

$$|0\rangle = \mathcal{N}_p \prod_p \left(\frac{1 + \hat{B}_p}{2} \right) |\Rightarrow\rangle = \mathcal{N}_p \left(1 + \sum_p \hat{B}_p + \sum_{p,p'} \hat{B}_p \hat{B}_{p'} + ... \right) |\Rightarrow\rangle. \tag{2.5}$$

4

$$\hat{B}_p \hat{B}_{p'} \hat{B}_{p^*} \hat{B}_{p''} \,|\Rightarrow\rangle \qquad\qquad \hat{B}_p \hat{B}_{p'} \,|\Rightarrow\rangle \qquad\qquad \hat{B}_p \hat{B}_{p'} \hat{B}_{p^*} \,|\Rightarrow\rangle$$
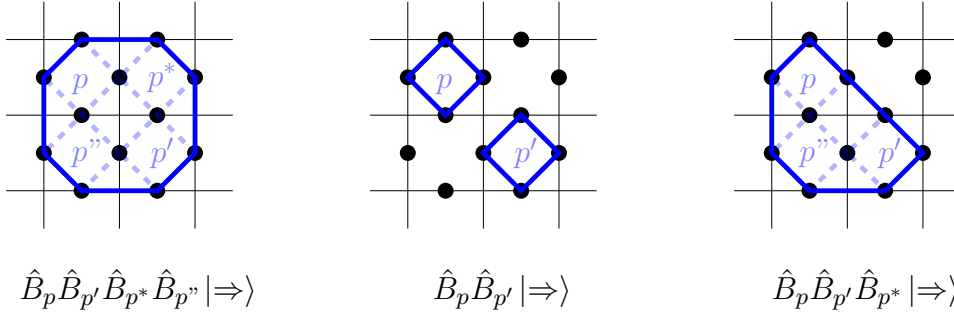
Figure 2.2: Possible loop-configurations of σ^z-operators created by different sequences of $\hat{B}_p$-operators acting on the reference state $|\Rightarrow\rangle$.

Each term in this sum creates closed loops of Pauli matrices σ_i^z acting on the edges of plaquettes, resulting in a superposition of every possible combination of those closed loops, sometimes called soup soup, like depicted in Figure 2.2. These loops are contractible, which means, that they can be constructed, by acting with B_p on the lattice. Another important property of the toric code on the square lattice is self-duality. This can be seen by shifting the grid in Figure 2.1, such that stars become plaquettes and vice versa.

2.1.2 Topologically ordered ground state

To illustrate the intrinsic topological order, it is beneficial to consider the toric code on a torus of genus $g = 1$. A superposition of closed loops still makes up the ground state, but on a torus, the periodic boundary conditions allow for new loops, namely global, non-contractible loops, as shown in Figure 2.3. These non-contractible loops of spin-flips run around the torus in poloidal and toroidal direction. A non-contractible loop can neither be created nor destroyed by local perturbations of $\hat{A}_s$- or $\hat{B}_p$-operators. With the reference state chosen in Equation 2.4, the presence of a loop can be probed by loop operators:

$$\hat{X}_{\mathcal{C}_j} = \prod_{i \in C_j} \sigma_i^x. \tag{2.6}$$

Since $\hat{X}_{\mathcal{C}_j}^2 = \mathbb{1}$, this operator takes the eigenvalue $x_j = \pm 1$. For $\mathcal{C}_j$ defined like in Figure 2.3, $X_{\mathcal{C}_1}$ detects the presence of a non-contractible loop in poloidal direction, while $X_{\mathcal{C}_2}$ indicates the presence of one in toroidal direction. If there is no global loop wrapping around the torus in poloidal direction, only non-contractible loops intersect $\mathcal{C}_2$. One can easily convince themselves, that a non-contractible, local loop always has an even number of intersections with $\mathcal{C}_2$ while global ones have an odd number of intersections. An exemplary global loop is depicted in Figure 2.3. Since one has $x_j = (-1)^{n_j}$, where n_j is the intersection number of $\mathcal{C}_j$ and loops in the ground state, this eigenvalue takes the value $x_j = -1$ if a global loop is present in the corresponding
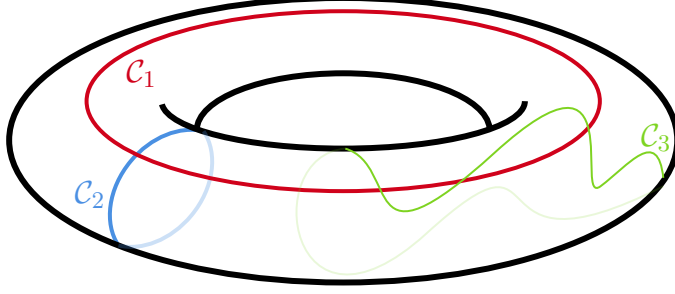
Figure 2.3: Toroidal and poloidal loops $\mathcal{C}_1$ and $\mathcal{C}_2$ in blue and red on the torus of genus $g = 1$. $\mathcal{C}_3$ is a deformed global loop.

direction and $x_j = +1$ if not. Using the ground state $|0\rangle$, which is a superposition of every possible loop configuration, the ground state on the torus can now be written as:

$$|n_1, n_2\rangle = \left(\frac{1 + n_1 \hat{X}_1}{2}\right)\left(\frac{1 + n_2 \hat{X}_2}{2}\right)|0\rangle, \qquad n_1, n_2 \in \{-1, +1\} \qquad (2.7)$$

Now $|0, +1, -1\rangle$ denotes the ground state, in which there is no loop in poloidal direction, while there is one in toroidal direction. While this loop can be deformed by the underlying local loops in the loop soup, as indicated in Figure 2.3, it always stays global. Since global loops cannot be created or destroyed locally, the Hilbert space $\mathcal{H}$ is separated into distinct subspaces. The ground-state degeneracy is 2^{2g}, where g is the genus of the torus. Thus the degeneracy of the ground state depends of the topology of the system, which strongly suggests the presence of topological order [31, 32].

One can also understand these non-contractible loops as additional degrees of freedom, which compensate for the ones, that are lost, since for the ground state on the torus one has:

$$\prod_s \hat{A}_s = \prod_p \hat{B}_p = \mathbb{1}. \qquad (2.8)$$

This relation can be explained by the fact that each spin is always part of two stars and two plaquettes. This means $\prod_s \hat{A}_s$ and $\prod_p \hat{B}_p$ act twice on every spin with $(\sigma^\alpha)^2$.

It will become evident in chapter 3, that the operators which we use for analysis of the ground state and the single-particle subspace are acting on strictly finite clusters of the model. Choosing a right basis, as will be done in subsection 3.2.3, we can disregard the underlying loops, such that it is possible to analyze the model exclusively in one subspace, for example the subspace with the ground state $|0, +1, +1\rangle$, where no global loops are present.
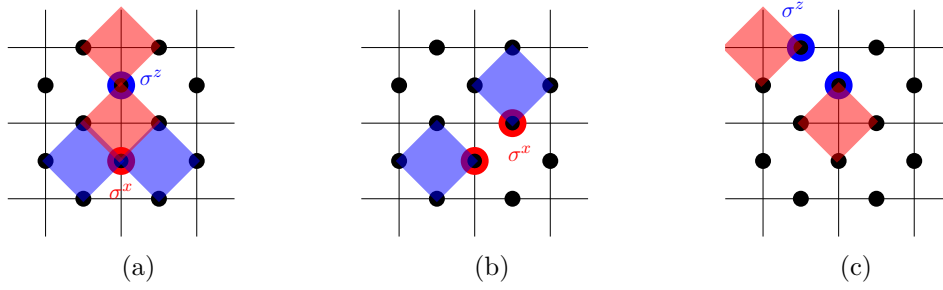
Figure 2.4: (a) Creation of a flux and charge-pair by acting with σ^x and σ^z respectively. (b) Moving one of the created fluxes by acting with σ^x on spin contained in an excited plaquette. (c) Moving one of the created charges by acting with σ^z on a spin contained in an excited star.

2.1.3 Elementary excitations

As discussed in the previous section, the ground-state manifold consists of states, in which all star- and plaquette operators $\hat{A}_s$ and $\hat{B}_s$ have the eigenvalue $a_s = b_p = +1$. Excitations, which are referred to as quasi-particles, arise, if single stars or plaquettes have an eigenvalue of -1. Conventionally, star-excitations are called 'charges', while plaquette-excitations are called 'fluxes'. These excited states can be obtained pairwise by acting with σ^α on a spin on the ground state. Acting with σ_j^x on a spin j in the ground state, for example, would create two fluxes on the neighbouring plaquettes, since here one has $\{\sigma^x, \hat{B}_p\} = 0$ for $j \in p$, while for every other plaquette with $j \notin p$, one has $\left[\sigma_j^x, \hat{B}_p\right] = 0$. The same relations hold true for σ^z and $\hat{A}_s$ and associated charge excitations. Acting with $\sigma^y = i\sigma^x\sigma^z$ on a spin creates both particle-pairs on its neighbouring sites, since for these stars and plaquettes, σ^y anti-commutes with $\hat{A}_s$ as well as $\hat{B}_p$. The discussed commutation-relations are visualized in Figure 2.4a.

The particle-pairs can be destroyed again, by acting with the same σ^α on the same spin. Since acting with σ^α flips the eigenvalue of adjacent stars or plaquettes, particles can also be moved that way, like depicted in Figure 2.4b and 2.4c. To analyze second-order phase transitions, the behaviour of a single particle can be investigated. Since particles are always created pairwise, one has to move one particle of the pair sufficiently far away with a string of σ^α-operators. Thus the sole particle can be studied, while one still has to keep the operator-string in mind. The string, on which one particle was moved away, has to be considered, since charges and fluxes obey unconventional mutual exchange statistics. This can be seen in the exchange statistics of two particles, as depicted in Figure 2.5.

In 2.5a a pair of fluxes was created by acting with $\hat{a}_f = \sigma_3^x$ on the ground state, creating the state $|\Psi_{\text{initial,f}}\rangle = \hat{a}_f |0\rangle$. Now these two particles can be exchanged the by following exchange operator

$$\hat{e}_f = \sigma_4^x \sigma_3^x \sigma_2^x \sigma_1^x.$$

Figure 2.5: (a) Initial state, where a flux-pair has been created by acting with σ_3^x on the ground state. (b) Exchange both fluxes by sequence of σ_i^x-operators.
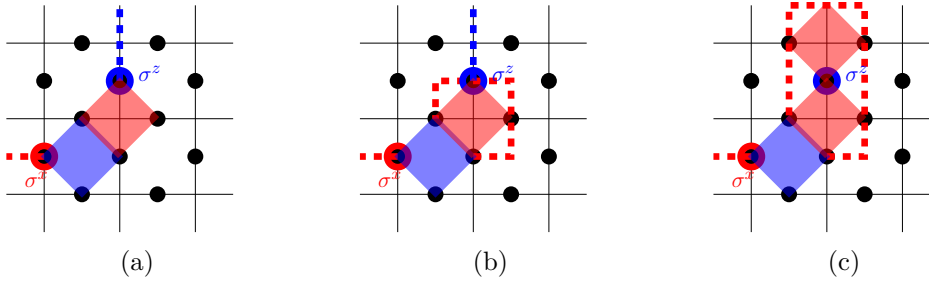

Figure 2.6: (a) Initial state, where one flux and one charge are brought together by their respective string operators. (b) Winding a flux around one charge. The string of σ^x-operators (red) intersects the string of σ^z-operators (blue) once. (c) Winding a flux around two charges. The string of σ^x-operators intersects the string of σ^z-operators an even number of times.

Since one has $[\hat{e}_{\mathrm{f}}, \hat{a}_{\mathrm{f}}] = 0$, the resulting state after an exchange process reads

$$|\Psi_{\mathrm{final,\ f}}\rangle = \hat{e}_{\mathrm{f}}\hat{a}_{\mathrm{f}}|0\rangle = \hat{a}_{\mathrm{f}}\hat{e}_{\mathrm{f}}|0\rangle = |\Psi_{\mathrm{initial,f}}\rangle.$$

The same relations hold for the exchange of a charge-pair, due charge-flux symmetry. The exchange of particle pairs shows, that these pairs obey bosonic statistics, if exchanged within the same particle-type. More unconventional statistics arise from mutual exchange of charges and fluxes. While charges and fluxes can not be exchanged per se, they can be moved around each other to exhibit new behaviour. Examples of winding processes can be seen in Figure 2.6. From the ground state, particle-pairs of each kind are created, which can be moved around with strings, such that the initial state is created by the operator $\hat{a}$, depicted in 2.6a. Moving one particle around another particle of a different kind can yield a sign for the wave-function. In winding processes like in 2.6b the σ^x and σ^z strings cross. At the intersection they act on the same spin, for which one has $[\sigma_i^x, \sigma_i^z] \neq 0$. The winding of a flux f can by expressed by the following operator

$$\hat{w}_{\mathrm{f}} = \sigma_4^x\sigma_2^x\sigma_1^x\sigma_3^x.$$

8

One can easily convince themselves, that $\hat{a}$ and $\hat{w}_f$ do not commute, if they share an odd number of spins. For the case depicted in 2.6b this results in following state after one winding process:

$$|\Psi_{\text{final},f}\rangle = \hat{w}_f \hat{a} |0\rangle = -\hat{a} |0\rangle = -|\Psi_{\text{initial},f}\rangle.$$

Here, the operator $\hat{a}$ contains all operators, that create the state depicted in 2.6a from the ground state. One can see, that the wave function gains a negative sign after winding one flux around a charge. It should be noted, that it is possible to wind fluxes around charges, without gaining a phase, by choosing a winding-path, that does cross any other σ^x-string zero or an even number of times. For that, the winding path could, for example, enclose both charges of the charge-pair, like seen in 2.6c. Exchanging fluxes and charges in this scenario results in the same exchange behaviour. Particles with this property are called Abelian anyons [5].

2.1.4 Magnetic field

The goal of this thesis its to investigate the perturbed topological phase. This perturbation is achieved by introducing a magnetic field. Generally each field-direction is considered, by perturbing the toric code with $-\sum_{i,\alpha} h_\alpha \sigma_i^\alpha$, where $\alpha \in \{x, y, z\}$ is the direction of the uniform magnetic field. The field term acts on every spin site i. The Hamiltonian now reads:

$$\hat{H} = -J_s \sum_s \hat{A}_s - J_p \sum_p \hat{B}_p - \sum_{i,\alpha} h_\alpha \sigma_i^\alpha. \tag{2.9}$$

This model is no longer exactly solvable. For specific cases, it is possible to map the system onto another model, for which the properties are already known. For a single parallel field, meaning h_x or h_z, Trebst et al. [15] proposed a mapping of the toric code in a single parallel field in x- or z-direction to the transverse field Ising model on a 2-dimensional square lattice. For this, one has to set $J_p \gg J_s, h$, such that the number of plaquette excitations is conserved. In the flux-free subspace with $b_p = +1$ for all plaquettes p, the effective Hamiltonian can then be written as:

$$\hat{H}_{\text{eff}}^z = -J_s \sum_s \hat{A}_s - h_z \sum_i \sigma_i^z - J_p N_p. \tag{2.10}$$

If one considers the model now on a dual lattice, where every star is a pseudospin site with $\hat{A}_s \to \tau_s^z$, while every original spin site is now considered a nearest neighbour link of the new, dual lattice with $\sigma_i^z \to \tau_s^x \tau_{s'}^x$ where s and s' are stars sharing the spin site i, one gets the following form of the Hamiltonian:

$$\hat{H}_{\text{dual}}^z = -J_s \sum_s \tau_s^z - h_z \sum_{<s,s'>} \tau_s^x \tau_{s'}^x. \tag{2.11}$$

The lattice and its dual counterpart can be seen in Figure 2.7.

<div align="center">(a)   (b)</div>

Figure 2.7: (a) The toric code on the square lattice with marked stars. (b) Dual lattice where the stars are lattice sites of again a square lattice, while original spin-sites lie on the bonds.

Trebst et al. [15] then mapped this quantum Ising model to a classical $(2 + 1)$-dimensional Ising model, which describes the continuous magnetic phase transition of the 3D-Ising model. While this mapping suffices for a single, parallel field, another mapping is needed to fully describe the system with arbitrary field directions. To do this Tupitsyn et al. [20] proposed a mapping of the toric code in a parallel field, meaning h_x- and h_z-fields are turned on simultaneously, to an anisotropic, three-dimensional $\mathbb{Z}_2$ gauge Higgs model. For this, the following Hamiltonian was considered:

$$\hat{H} = -J_s \sum_s \hat{A}_s - J_p \sum_p \hat{B}_p - h_x \sum_i \sigma_i^x - h_z \sum_i \sigma_i^z. \tag{2.12}$$

Introducing pseudo spin-1/2-degrees of freedom μ, that act on stars s, makes this mapping possible, while also enlarging the Hilbert space $\mathcal{H}$. Thus one has to only consider physical states, such that $\mu_s^x |\Psi\rangle = |\Psi\rangle$. Introducing the gauge-condition that physical states must be invariant under $\mu_s^x \hat{A}_s$, one can identify $\mu_s^x = \hat{A}_s$. Realizing, that acting with σ_i^z, a field-term in Equation 2.12, on a spin flips the eigenvalues of the neighbouring stars, lets us write this operator as $\sigma_i^z = \mu_s^z \sigma_{<s,t>}^z \mu_t^z$, where s and t are neighbouring stars that are connected by the physical spin i, denoted by $<s,t>$. Using these relations, the Hamiltonian in Equation 2.12 can be rewritten:

$$\hat{H} = -J_s \sum_s \mu_s^x - J_p \sum_p \hat{B}_p - h_x \sum_i \sigma_i^x - h_z \sum_{<s,t>} \mu_s^z \sigma_{<s,t>}^z \mu_t^z. \tag{2.13}$$

Tupitsyn et al. mapped this 2D quantum Hamiltonian onto a 3D classical Ising-type model, which recovered the anisotropic Z2-gauge Higgs model [20]. The resulting phase-diagram for $J_s = J_p$ is depicted in Figure 2.8. One can see, that the topological phase is robust under certain magnetic perturbations. For large field-strengths, the system realizes a polarized phase. Since this model exhibits a self-duality symmetry, the phase-diagram is symmetric with regard to the self-duality line $h_x = h_z$, which intersects the pink and red lines at the so called multicritical point.
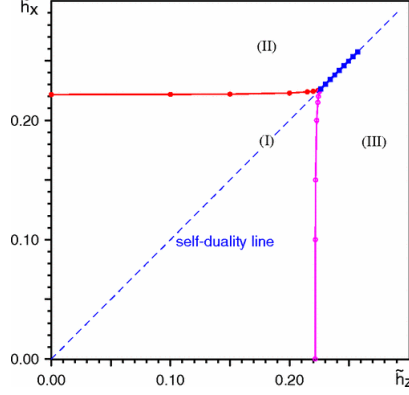
Figure 2.8: Figure taken form [20]. The topological phase is labeled by (I), while the polarized phase is labeled by (II) and (III). The self-duality line marks the case $h_x = h_z$. The red and pink lines and the circles on them represent second order 3D-Ising phase transition, while the blue squares beyond the topological phase mark a first-order phase transition.

One notices, that in Equation 2.13 some parts remain unchanged. To perform a graph expansion for the all field-directions, we have to bring these parts to the same form as before. For this, another dummy spin variable μ_p is introduced, that acts on the plaquettes. Following the same considerations like before, one can write the Hamiltonian in the following form, while setting $J_s = J_p = J$:

$$\hat{H} = -J\sum_s \mu_s^x - J\sum_p \mu_p^x - h_x \sum_{<p,q>} \mu_p^z \sigma_{<p,q>}^x \mu_q^z - h_z \sum_{<s,t>} \mu_s^z \sigma_{<s,t>}^z \mu_t^z. \qquad (2.14)$$

Here the neighbouring plaquettes p and q are connected by a spin i, which is denoted by the index $< p,q >$. It is also possible to write the full Hamiltonian 2.9 with all field direction in this form. For this one has to consider the effect of σ_i^y on the μ_s and μ_p dummy spins. By acting with σ_i^y on a spin i, the eigenvalues of two neighbouring star-operators s and t and the two neighbouring plaquette-operators p and q get flipped, which lets us identify $\sigma_i^y = i\mu_p^z \mu_s^z \sigma_{<s,t,p,q>}^x \sigma_{<s,t,p,q>}^z \mu_t^z \mu_q^z$. Substituting this into the Hamiltonian 2.9 results the following Hamiltonian:

$$\hat{H} = -J\sum_s \mu_s^x - J\sum_p \mu_p^x - h_x \sum_{<p,q>} \mu_p^z \sigma_{<p,q>}^x \mu_q^z - h_z \sum_{<s,t>} \mu_s^z \sigma_{<s,t>}^z \mu_t^z \qquad (2.15)$$
$$- ih_y \sum_{<s,t,p,q>} \mu_p^z \mu_s^z \sigma_{<s,t,p,q>}^x \sigma_{<s,t,p,q>}^z \mu_t^z \mu_q^z.$$

Both Hamiltonians 2.14 and 2.15 mostly act on two different lattices, like seen in Figure 2.9, only the original spins σ_i connect the two lattices. For both Hamiltonians the μ-pseudospins can be coupled ferro- or antiferromagnetically, depending on the sign of h_x, h_y, and h_z. But due to the square lattice being bipartite, the system is invariant under sign-change of h_x, h_y, or h_z.
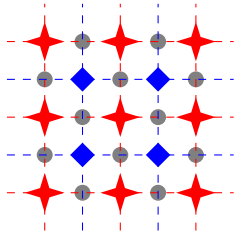
11

Figure 2.9: The dual lattice of the complete toric code, where stars and plaquettes form the sites, while original spin-sites lie on the bonds.

It should be mentioned, that the case for $h_x = h_z = 0$ and $h_y \neq 0$ can by mapped onto the Xu-Moore model, as shown by Vidal et al. in [17]. Here the self-duality can be exploited to find that the phase transtition between the topological phase and the polarized one lies at $J = h_y$. The phase transition is of first order.

Kamfor, Schmidt et al. [21, 25] also analyzed the toric code for a uniform, three-dimensional magnetic field. The resulting three-dimensional phase diagram is depicted in Figure 2.10. There, for $h_y = 0$, one recovers the same phase diagram as is Figure 2.8, if one rescales the field strengths. Since in [25], $J_p = J_s = \frac{1}{2}$ was chosen one also recovers the phase transition at $(h_x, h_y, h_z) = (0, \frac{1}{2}, 0)$, which mirrors finding for the Xu-Moore model [17]. It becomes evident, that the topological phase is robust not only under magnetic perturbation with parallel fields, but also for uniform fields. In this thesis, we will try to confirm results obtained by Kamfor, Schmidt et al. [21, 25]. Our findings for the toric code on a square lattice are presented and compared to [25] and [21] in section 4.2. For our analysis, we also chose $J = J_p = J_s$.

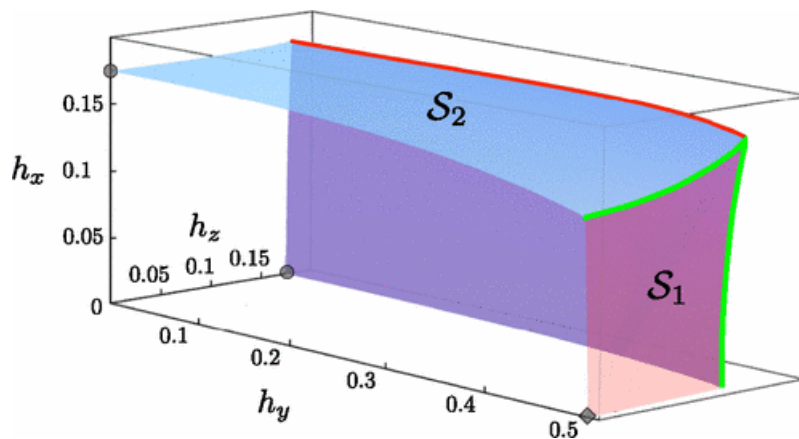Figure 2.10: Figure taken from [21]. The topologically-ordered phase is contained by second-order phase transition sheet $\mathcal{S}_2$ and a first-order phase transition sheet $\mathcal{S}_1$. The red line, which runs from $h_y = 0$ to $h_y = 0.46$ [21], shows the course of the multicritical point for increasing h_y. The green lines show the intersection between sheets $\mathcal{S}_1$ and $\mathcal{S}_2$.
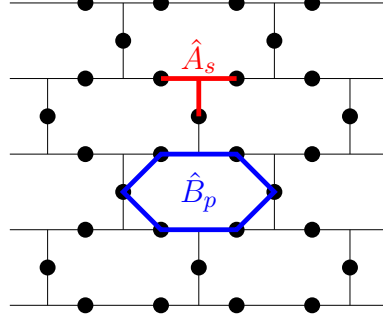
Figure 2.11: Honeycomb lattice with plaquettes p (blue) and stars s (red) and their respective operators $\hat{B}_p$ and $\hat{A}_s$

2.2 The toric code on a honeycomb lattice

Besides the toric code on a square lattice, we also investigate the toric code on the honeycomb lattice, which is depicted in Figure 2.11 and has not been studied before in detail. While most properties are the same like in the previous section, some important properties change. Namely, symmetry and self-duality.

The breaking of self-duality can be easily understood, by considering stars s and plaquettes p or their corresponding operators:

$$\hat{A}_s = \prod_{i \in s} \sigma_i^x = \sigma_j^x \sigma_k^x \sigma_l^x$$

$$\hat{B}_p = \prod_{i \in p} \sigma_i^z = \sigma_j^z \sigma_k^z \sigma_l^z \sigma_m^z \sigma_n^z \sigma_o^z$$

This model cannot be self-dual, since the star- and plaquette-operators cannot be exchanged. Hence, we do not expect an invariance under $h_x - h_z$-exchange and thus no self-duality line like in Figure 2.8. The asymmetry becomes evident, if one inspects the dual lattices. In Figure 2.12a the dual plaquette lattice is depicted. One can see, that the plaquette-excitation move on a triangular lattice. Figure 2.12b depicts the dual lattice of plaquettes and stars. Using the same considerations like in subsection 2.1.4, one can rewrite the Hamiltonian into the following form:

$$\hat{H} = -J_s \sum_s \mu_s^x - J_p \sum_p \mu_p^x - h_x \sum_{<p,q>} \mu_p^z \sigma_{<p,q>}^x \mu_q^z - h_z \sum_{<s,t>} \mu_s^z \sigma_{<s,t>}^z \mu_t^z.$$

p and q are neighbouring plaquettes and s and t are neighbouring stars. Here one can see, that the pseudo-spins μ can realize an antiferromagnetic or ferromagnetic coupling, depending on the sign of h_x or h_z. For the star-spins μ_s, which lie on a hexagonal lattice, this makes no difference, due to invariance of the model under sublattice-rotation. Hence we expect the same behaviour for negative and positive h_z. For the plaquette-spins, one encounters geometrical frustration for the antiferromagnetic case, meaning for negative h_x. Thus a different behaviour is expected for different signs of h_x. By setting h_x or
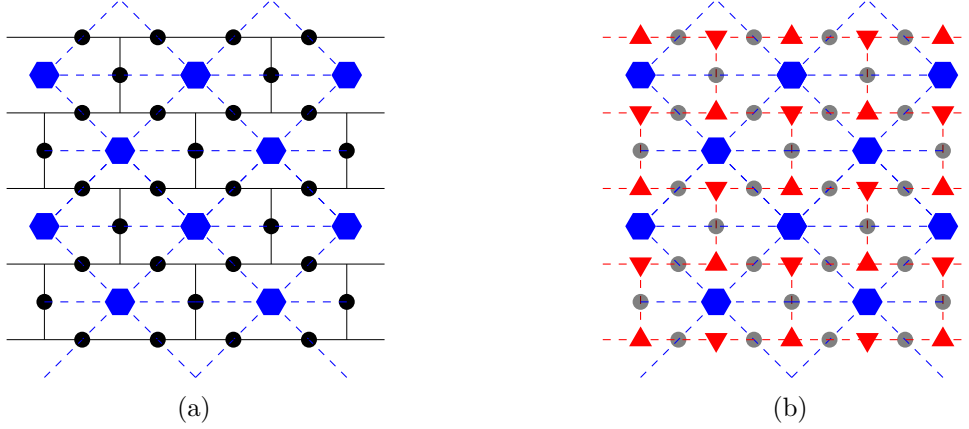
Figure 2.12: (a) Dual lattice of the plaquettes on the honeycomb lattice. (b) Dual lattice of both stars and plaquettes, where stars and plaquettes are sites of the lattice, while the original spin-sites lie on bonds.

h_z to zero, one regains the transverse field Ising model on a hexagonal or triangular lattice, if one considers only select subspaces with $b_p = +1$ for all p or $a_s = +1$ for all s. The transverse field Ising model on the hexagonal lattice possesses a phase transition, that belongs to the 3D-Ising universality class for ferromagnetic and antiferromagnetic coupling due to bipartitness [33]. The transverse field Ising model on a triangular lattice realizes a phase transition in the 3D-Ising class for ferromagnetic coupling [33] while for the antiferromagnetic case, its phase transition belongs to the 3D-XY universality class [34]. Considering a transverse field h_y yields the same Hamiltonian as for the square lattice model. For the analysis of the toric code on the honeycomb lattice, we again chose $J = J_p = J_s$.

3. Perturbative continuous unitary transformations and linked-cluster expansion

In this chapter the various series and cluster expansion methods are explained. To motivate the linked cluster approach, the perturbative continuous unitary transformations are explained first. With the linked cluster theorem the graph-decomposition can be used. The results from this analysis are then evaluated with Padé and DlogPadé approximations, which are explained in the next chapter.

3.1 PCUT

In this section we will give a short overview on the perturbative continuous unitary transformation method. For this a short summary of the underlying method, namely the continuous unitary transformation, is provided, before proceeding to the perturbative method.

3.1.1 CUT

The continuous unitary transformation (CUT) was first introduced simultaneously by Wegner [35] and Głazek et al. [36]. The goal of this transformation is to transform a Hamiltonian, such that $H \to UHU^{\dagger}$, where U is a unitary matrix. To gain the effective Hamiltonian H_{eff}, which ideally simplifies the eigenvalue-problem and is (block-)diagonal, this transformation is done continuously, by introducing the flow-parameter l, such that $H(l=0) = H_0$ and $H(l=\infty) = H_{\text{eff}}$. The transformation then reads:

$$H(l) = U(l)H_0 U^{\dagger}(l). \tag{3.1}$$

The unitariy transformation $U(l)$ is defined by an anti-hermitian generator $\eta(l)$:

$$\frac{dU(l)}{dl} = \eta(l)U(l). \tag{3.2}$$

The flow-equation follows:

$$\frac{dH(l)}{dl} = [\eta(l), H(l)].$$

(3.3)

The form of this generator η governs the form that H_{eff} takes. Uhrig and Kettner [26] proposed a new generator, such that the effective Hamiltonian becomes block diagonal. More specifically, the effective Hamiltonian becomes excitation or quasi-particle-conserving. The quasi-particle generator they proposed takes the following form:

$$\eta_{i,j}(l) = \text{sgn}(i-j)h_{i,j}(l).$$

(3.4)

Here i and j are numbers of particles, while $h_{i,j}$ is a block of $H(l)$, in which j quasi-paricles are created and i are destroyed.

3.1.2 Perturbative CUT

The CUT has been studied for a perturbative ansatz [26, 27]. For some systems, it is possible to use a perturbative, model-independent approach. The perturbative CUT (pCUT) formalism requires a Hamiltonian of the form:

$$H = H_0 + \lambda V.$$

(3.5)

Here H_0 is the unperturbed Hamiltonian, while λ is a small perturbation parameter and V is the perturbation. This Hamiltonian must fulfill two conditions:

The first requirement is, that H_0 has an equidistant spectrum, which is bounded from below. With a quasi-particle counting operator Q, for which $Q|i\rangle = i|i\rangle$, where $|i\rangle$ is a state with i quasi-particles, one can write

$$(\hat{H}_0 - E_0)|i\rangle = \epsilon Q|i\rangle = \epsilon i|i\rangle$$

(3.6)

The second condition is, that the perturbation can be written as

$$V = \sum_{n=-N}^{N} T_n,$$

(3.7)

where the operator T_n creates n quasi-particles. For $n < 0$, the operator annihilates $|n|$ particles, while T_0 does not change the particle number. Thus the relation $[T_n, Q] = nT_n$ holds. N is the maximum number of quasi-particles, that are destroyed or created by H. The resulting Hamiltonian can be rewritten:

$$H(l) = H_0 + \lambda \sum_{n=-N}^{N} T_n = H_0 + \sum_{k=1}^{\infty} \lambda^k \sum_{|\mathbf{m}|=k} F(l, \mathbf{m})T(\mathbf{m}).$$

(3.8)

Here, $F(l, \mathbf{m})$ are real-valued functions, which can be determined analytically [26].

16

$T(\mathbf{m}) = T_{m_1} T_{m_2} T_{m_3} ... T_{m_k}$ is a product of the lenght $|\mathbf{m}| = k$. The vectorcomponents m_i are restricted to the number of particles that can by destroyed or created by H, while the total number of quasi-particles changes by $M(\mathbf{m}) = \sum_{i=1}^{k} m_i$. Using considerations from the previous chapter, the particle conserving generator now reads:

$$\eta(\lambda, l) = \sum_{n=1}^{\infty} \lambda^n \sum_{|\mathbf{m}|=n} \text{sgn}(M(\mathbf{m})) F(l, \mathbf{m}) T(\mathbf{m}). \tag{3.9}$$

Now $F(l, \mathbf{m})$ can be solved by using the flow-equation. The final expression for the effective Hamiltonian can now be given as:

$$H_{\text{eff}}(\lambda) = H_0 + \sum_{k=1}^{n_{order}} \lambda^k \sum_{|\mathbf{m}|=k, M(\mathbf{m})=0} C(\mathbf{m}) T(\mathbf{m}), \tag{3.10}$$

where $C(\mathbf{m}) = F(\infty, \mathbf{m})$. For an exact expression one needs $n_{order} = \infty$, while in reality this number is the highest order that is calculated and is restricted by computation time. The condition $M(\mathbf{m}) = 0$ can be motivated by the form of $F(l, \mathbf{m})$, which is only non-zero for $M(\mathbf{m}) = 0$ and $l \to \infty$. Another important property that comes from $F(l, \mathbf{m})$ is the linked cluster theorem [29]. To gain a better understanding, one can examine the T_n-operators more closely. T_n acts on the whole lattice, but excitations are only created/annihilated locally. Thus, T_n can be expressed as a superposition of many local $\tau_{n,i}$-operators, that act only on the lattice-site i [37]:

$$T_n = \sum_i \tau_{n,i}. \tag{3.11}$$

Inserting this into Equation 3.10 one gets:

$$H_{\text{eff}}(\lambda) = H_0 + \sum_{k=1}^{n_{order}} \lambda^k \sum_{|\mathbf{m}|=k, M(\mathbf{m})=0} C(\mathbf{m}) \sum_{i_1, i_2, ... i_k} \tau_{m_1, i_1} \tau_{m_2, i_2} ... \tau_{m_k, i_k}. \tag{3.12}$$

In the last sum one gets $\tau_{m_1, i_1} \tau_{m_2, i_2} ... \tau_{m_k, i_k}$. Here k τ-operators act locally on the lattice-site i_a. One can show, that these τ-operator-sequences only contribute, if all lattice-sites i_a are connected, meaning the operator sequence acts on one connected cluster. Thus, quantities for the thermodynamic limit can be calculated, by only considering the effective operators on finite clusters [29].

3.2 Linked-cluster expansion

In this section the linked-cluster expansion is explained on the basis of the toric code on the square lattice. The same considerations hold true for the honeycomb lattice.
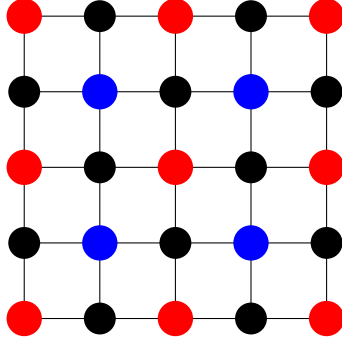
Figure 3.1: 5×5-cluster of the toric code on a square lattice, represented as a graph. Stars, plaquettes and spins are represented as red, blue and black nodes.

3.2.1 Graphs

Graphs are made up of nodes and edges. In our case the nodes are the sites of plaquettes, stars and spins. Interactions between these can be modelled as edges. The graph-representation of a cluster of the toric code on a square lattice is depicted in Figure 3.1. The respective Hamiltonian was already introduced in the previous section and reads:

$$\hat{H} = -J\sum_{s}\mu_s^x - J\sum_{p}\mu_p^x - h_x\sum_{<p,q>}\mu_p^z\sigma_{<p,q>}^x\mu_q^z - h_z\sum_{<s,t>}\mu_s^z\sigma_{<s,t>}^z\mu_t^z$$
$$-ih_y\sum_{<s,t,p,q>}\mu_p^z\mu_s^z\sigma_{<s,t,p,q>}^x\sigma_{<s,t,p,q>}^z\mu_t^z\mu_q^z.$$

This Hamiltonian consists of three different flavours of spins. μ_s and μ_p are different kinds of pseudo-spins, while σ denotes the physical spin. Interactions between different nodes are contained in the field-terms and can be understood by considering the effect of the perturbations on the ground state. The h_x-field-term $\mu_p^z\sigma_{<p,q>}^x\mu_q^z$ acts on a cluster depicted in Figure 3.2a. The h_z perturbation acts analogously, depicted in Figure 3.2b. The h_y-field combines these two, such that the cluster of nodes, on which it acts looks like Figure 3.2c. These graphs are the smallest units of larger graphs and are called bonds.

Since the toric code can be represented as a graph and we are using the pCUT-method, for which the linked cluster theorem holds, we only need to consider processes on connected graphs. Any process that acts on a disconnected cluster marked in Figure 3.3b will not contribute to any calculation, while a process acting on a connected graph, depicted in Figure 3.3a, will. Both graphs would only contribute in order 4 or higher,

18
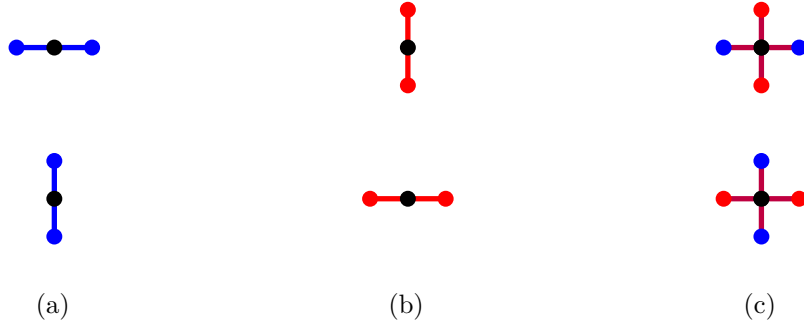
Figure 3.2: (a) Topologically equivalent bonds, made up of two plaquettes (blue) and a physical spin (black). (b) Topologically equivalent bonds, made up of two stars (red) and a physical spin (black). (c) Topologically equivalent bonds, made up of two plaquettes (blue) and a physical spin (black).

since both contain 4 bonds. This can be easily seen in Equation 3.12, since 4 different τ-operators are needed to act on these graphs.

(a) Connected Graph   (b) Disconnected Graph
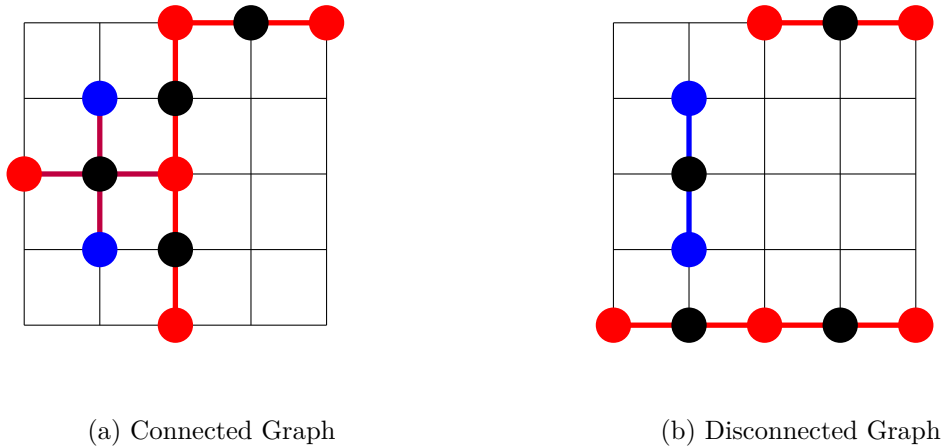
Figure 3.3: (a) A connected graph, where all nodes are connected. (b) A disconnected graph, where sets of nodes, which are connected to each other, are not connected.

3.2.2   Graph decomposition

Now it is of interest to calculate all graphs up to a certain order. This could be done by brute-force, which would be very costly in computation time and memory. For that reason, an implementation by Matthias Mühlhauser was used, to calculate only relevant

graphs. The basic steps of calculating the relevant graphs will be summarized here. A detailed description can be found in [28].

The starting point are the bonds depicted in Figure 3.2. From these graphs every other graph is iteratively calculated. For that, every kind of bond is added to existing graphs in every way, if the lattice allows this new configuration. This process is depicted Figure 3.4. Here bonds have been added to graphs of order 1, to create graphs, that contribute in order 2. Only topologically distinct graphs are depicted in each row, since topological equivalent structures lead to the same contribution. In the resulting graphs there are still topologically equivalent structures (e.g. the red and blue cross), which can be summarized to one graph, so that only 9 topologically distinct graphs remain. This process is repeated for every emerging graph up to the desired order. One can reduce redundancies by creating topologically invariant graphs only once.
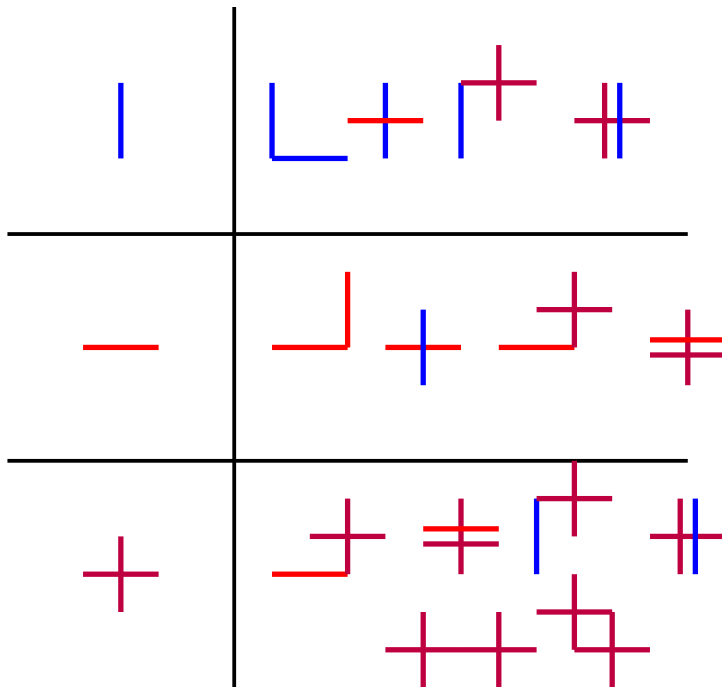
Figure 3.4: Sketches of bonds introduced in Figure 3.2. On the left, graphs contribute in order 1. On the right side of each graph of order 1, the corresponding graphs, that can be constructed by adding one bond, are sketched.

After determining the contributing graphs, their contribution has to be calculated. For this, the effective Hamiltonian is applied to each graph. Following the works of Gelfand et al. [29], for any observable $P(c)$ on a cluster c, one can find for $W(c)$, that

$$P(c) = W(c) + \sum_{c_{sub} \subset c} W(c_{sub}). \tag{3.13}$$

$W(c)$ is the weight of the cluster c, which will be used in Equation 3.18 to calculate the observable on the whole lattice $\mathcal{L}$. The sum runs over all subclusters which are

contained in the original cluster c. For the ground-state energy per site specifically, this expression then reads:

$$\langle 0_c | \frac{H_{\text{eff}}}{N} | 0_c \rangle = e(c) + \sum_{c_{sub} \subset c} e(c_{sub}) \tag{3.14}$$

$$= e(g_c) + \sum_{g_{sub} \subset g_c} n_g(g_{sub}) e(g_{sub}). \tag{3.15}$$

Here $e(c)$ is called the reduced energy of the cluster c, while $|0_c\rangle$ is the ground state on a cluster c. Equation 3.14 can be rewritten to 3.15, where the graph-representation was chosen. Now one has to consider $n_g(g_{sub})$, which is the number of times g_{sub} is contained in g. A graphical representation of a cluster in the graph-representation can be seen in Figure 3.5a, while the subclusters contained in it are depicted in Figure 3.5b. The whole graph only contributes in order six or higher. This is because every bond has to be acted upon twice, since particles are always created pairwise. It should be mentioned, that this condition only holds for clusters, which do not contain a loop [38]. An example of a τ-sequence of the lowest possible order, that acts on the whole cluster 3.5a is:

$$\tau_{A,-2}\tau_{B,0}\tau_{B,0}\tau_{C,0}\tau_{C,0}\tau_{A,+2}. \tag{3.16}$$

This operator-sequence creates a particle pair at the bond A. One particle is then moved twice on bond C and twice on bond B before returning to the initial bond A, where the pair is annihilated. Graphically, Equation 3.15 can the be represented in the following way:

$$\langle \_\bot\_ | H_{\text{eff}} | \_\bot\_ \rangle = e(\_\bot\_) + e(\text{———}) + e(\_\lrcorner) + e(\llcorner) + 2e(\text{—}) + e(|)$$

$$= e(\_\bot\_) + 3e(\text{———}) + 3e(\text{—}) \tag{3.17}$$

Since the topologically equivalent clusters have the same contribution, they can be summed up. To now calculate the observable on the whole lattice $\mathcal{L}$, one has to sum over all clusters:

$$\frac{P(\mathcal{L})}{N} = \sum_c L(\mathcal{L}, c) W(c). \tag{3.18}$$

Here N is the number of physical sites and $L(\mathcal{L}, c)$ is the lattice constant of the cluster c, which gives the number of possible embeddings of c in $\mathcal{L}$. Summarized, it is possible to calculate the ground-state energy per site of a lattice with

$$e_0(\mathcal{L}) = \sum_c L(\mathcal{L}, c) e(c) \tag{3.19}$$

by summing up every reduced energy of all clusters. Thus, it is sufficient to calculate the reduced energy of every existing cluster once and use the results to calculate the observable in the end.

Just like the ground-state energy, the reduced energies of a particle hopping from one site to another one can be calculated. Here the single-particle sector of the Hilbertspace
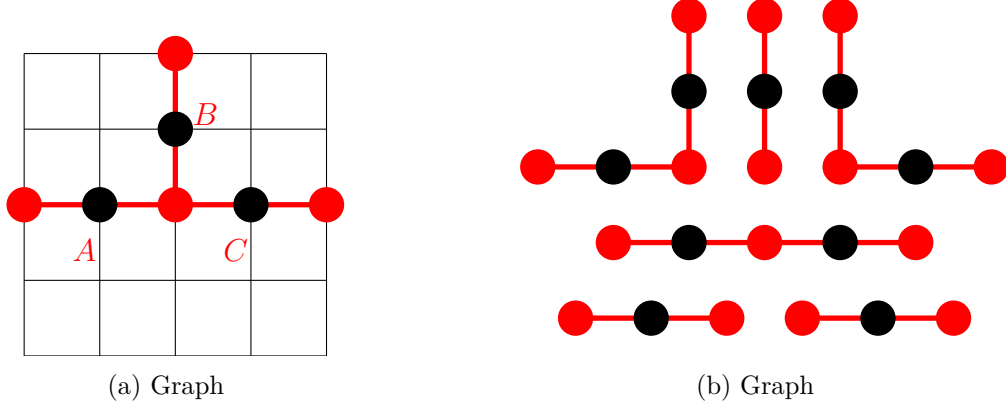
(a) Graph

(b) Graph

Figure 3.5: Representation of a graph-decomposition for a simple graph in (a) into its sub-graphs in (b)

$\mathcal{H}_1$ is of interest:

$$H_{\text{eff,1qp}} = H_0 + H_1 \tag{3.20}$$
$$H_0 \ket{i} = E_0 \ket{i} \tag{3.21}$$
$$H_1 \ket{i} = \sum_j t_{ij} \ket{j}. \tag{3.22}$$

Here $\ket{i}$ is a one-quasi-particle state, in which the quasi-particle is located at site i. H_0 acts on the zero-particle subspace, H_1 acts on the one particle subspace and moves the quasi-particle around. For N quasi-particle sites, the Fourier transform of $\ket{i}$ reads:

$$\ket{\mathbf{k}} = \frac{1}{\sqrt{N}} \sum_i e^{i\mathbf{k}\mathbf{r}_i} \ket{i} \tag{3.23}$$

Applying the one-quasi-particle to this Fourier transform in momentum space, one gets

$$H_0 \ket{\mathbf{k}} = E_0 \ket{\mathbf{k}} \tag{3.24}$$

For the zero-particle subspace. For the single-particle subspace, one gets

$$H_1 \ket{\mathbf{k}} = \frac{1}{\sqrt{N}} \sum_j \sum_i t_{ij} e^{i\mathbf{k}\mathbf{r}_i} \ket{\mathbf{r}_i + \mathbf{r}_j} = \left(\sum_i t_{ij} e^{-i\mathbf{k}\mathbf{r}_i} \right) \frac{1}{\sqrt{N}} \sum_j e^{i\mathbf{k}\mathbf{r}_j} \ket{r_j}$$
$$= \sum_i t_{\mathbf{r}} \cos(\mathbf{k}\mathbf{r}) \ket{k} = \omega(\mathbf{k}) \ket{\mathbf{k}}, \tag{3.25}$$

where the symmetry $t_{\mathbf{r}} = t_{-\mathbf{r}}$ was used, to eliminate the complex part of the exponential function. To calculate the dispersion, the different hopping elements $t_{\mathbf{r}}$ have to be calculated. To simplify the notation, $t_{\mathbf{r}} = t_{\mathbf{r}_i} - t_{\mathbf{r}_j} = t_{ij}$ is rewritten. Using 3.20 and
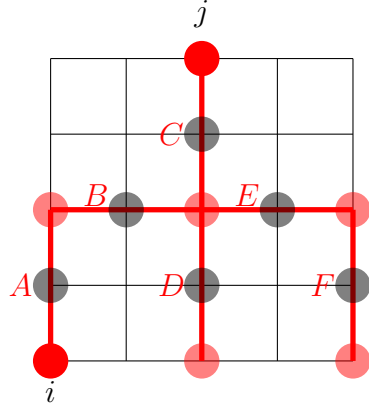
Figure 3.6: Possible cluster for a hopping process from site i to j or vice versa.

3.21, the hopping element can be then calculated:

$$t_{ij} = \langle i | H_1 | j \rangle. \tag{3.26}$$

Using the same considerations as before, we can use linked-cluster expansion to calculate these quantities. For this, one again considers clusters or hopping paths, on which the particles moves form site i to site j, which are represented as graphs. One such cluster is shown in Figure 3.6. Using the graph representation of this cluster, we can write

$$\langle i_c | H_1 | j_c \rangle = t_{i,j}(g) + \sum_{g_{sub} \subset g} n_g(g_{sub}) t_{ij}(g_{sub}), \tag{3.27}$$

which are the reduced contributions of single graphs to the hopping amplitude. $|j_c\rangle$ is a one particle state on the cluster c with the particle at site j. The whole hopping amplitude can be written as:

$$t_{i,j}(\mathcal{L}) = \sum_c L_{ij}(\mathcal{L}, c) t_{ij}(c). \tag{3.28}$$

Here $t_{ij}(c)$ is the reduced energy of the hopping process form site i to site j on the cluster c, while $L_{ij}(\mathcal{L}, c)$ is the lattice constant that only considers clusters that connect site i and j. For Figure 3.6, a potential τ-sequence of the lowest possible order of 9 would be:

$$\tau_{A,0} \tau_{B,0} \tau_{C,0} \tau_{F,-2} \tau_{E,0} \tau_{D,0} \tau_{E,-2} \tau_{D,2} \tau_{F,2}. \tag{3.29}$$

Here it is of interest, that bonds that lie on the direct path from i to j, such as bonds A, B and C, are only acted upon once, since one particle was already present, while excess bonds like D, E and F, which are not directly required for the hopping, have to be acted on twice. This condition again does not hold for loops. One can use this property that some bonds have to be perturbed twice to reduce the calculation time [38].

23

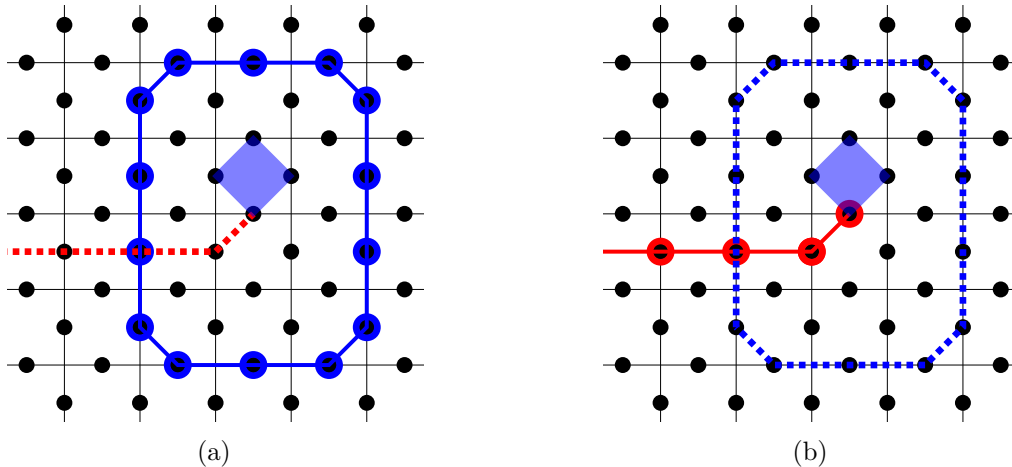Figure 3.7: (a) Visible loop of σ^z-matrices, depicted as a solid line. The loop consists of spin-flips, marked by blue circles. The flux is moved by an invisible string that only yields signs. (b) Invisible loop of σ^z-matrices, depicted as a dotted line. The reference state is chosen as an eigenstate of this operator sequence. The flux is moved by a string of σ^x-operators, which flip spins, marked by red circles.

3.2.3 Linked-cluster expansion in a topological phase

Another way to reduce computation time is to choose the right gauge. This is especially interesting for the non-zero particle subspaces, since, depending on the initially chosen reference state, different problems arise. For this a cluster of the toric code in the ground state is chosen, on which a particle-pair is created. One particle is then moved sufficiently far away, such that only one particle and a operator-string remains relevant inside the considered cluster. Since the ground state consists of closed loops, the interaction of the strings and loops has to be considered [25].

The first option would result in "invisible" strings that move the particle (fluxes). For this, the reference basis would be chosen such that acting with σ^x on a spin would not result in a spin-flip. Hence, the chosen basis would be the basis of the σ^x-operator. Due to the commutation-rules mentioned in subsection 2.1.3, one can gain a negative sign, if the path of σ^x operators crosses a string of σ^z-operators, like depicted in Figure 3.7a. Since the ground state consists of a superposition of loops, one has to differentiate the processes, in which the particle-path crosses such loops an odd number of times and the wave-function gains a negative sign, or in which the particle crosses loops an even number of times and the wave-function gains no sign. These different cases have to be detected.

The second option results from another choice for the reference state, in which the flux is moved by a string of operators, that flip the spin they act on, while the σ^z operators of the loops of only yield signs. For that, the reference state is chosen to be an eigenstate of the σ^z-operators. Now the particle can be moved into a loop, where its wavefunction does not pick up a sign. The process is depicted in Figure 3.7b. While

this option is preferential for the one-quasi-particle space, additional statistics have to be considered for additional particles.

Kamfor, Schmidt et al. [21, 25] investigated the toric code on square lattice using a finite-lattice method [24], where they applied perturbation theory directly to a cluster and did not consider graphs. They chose the first option, where a post processing was necessary. This was done in order to perform calculations in the two-particle subspace and consumed roughly $5 \cdot 10^4$ CPU-hours and yielded dispersions of single particles up to order 8 for the three-dimensional magnetic field. In this work, the second gauge-option was chosen, since only the single-particle subspace was considered. This allowed us to calculate the single-particle dispersion for the same model up to order 9 in only about $1 \cdot 10^2$ hours.

4. Results

In this chapter the results of the linked-cluster expansion and applications of the pCUT-method are extrapolated and discussed. Our results on the toric code on the square lattice are compared to [21]. Here we are especially interested in the development of the multicritical point $h_x = h_z$ for increasing h_y. In [21] it was suggested, that for certain h_y, a new universality class is realized. After investigating the toric code on the square lattice, we will consider it on a honeycomb lattice. For this model we will analyze certain cases, such that a phase diagram for an uniform magnetic field can be constructed.

4.1 Extrapolation methods

The nature of the perturbation theory used in this work and explained in subsection 3.1.2 leaves us with analytical expressions of the form

$$f_N(h) = \sum_{j=0}^{N} a_j h^j, \tag{4.1}$$

where a_j are real coefficients and h is the perturbation parameter, which in this case is the magnetic field strength. As seen in Figure 4.1, the polynomial functions converge to a function of infinite order, but due to high computation time, only finite orders of perturbation can be considered. To gain further understanding of the behaviour of the analytical series, we use the method of Padé extrapolation, which extrapolates $f_N(h)$ by a rational function. An advantage of a rational extrapolation is, that phase transitions and critical exponents can be easier obtained, since the condensation of an elementary excitation is a clear indication of a quantum phase transition where the mass gap obeys the following proportionality near the quantum-phase-transition point:

$$\Delta \propto (h - h_c)^{z\nu} \tag{4.2}$$

Here h_c is the critical field strength, at which the gap vanishes, while the critical exponent νz describes the systems behaviour near the phase transition, where z is the dynamical exponent and ν is another critical exponent [39]. In the next sections, the
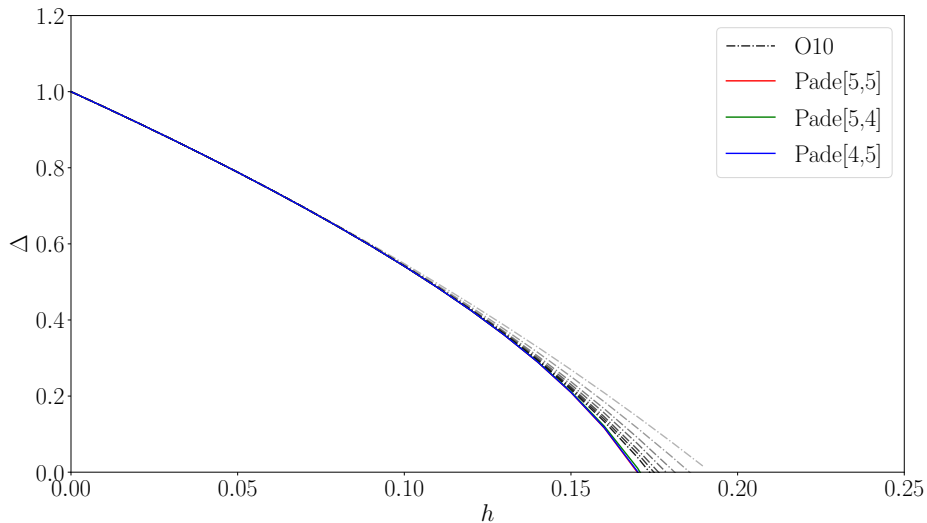
Figure 4.1: The single particle gap Δ for the toric code on a square lattice for their corresponding single, parallel field h. The black dotted lines represent polynomial expressions of $\Delta(h)$. The least opaque line depicts order 4, while opacity increases up to the most opaque line, representing order 10. Coloured lines represent the Padé approximants

Padé and DLogPadé methods are summarized. A more detailed description of this method is provided by Guttmann in [40].

The Padé extrapolation of Equation 4.1 is given by

$$P[L,M]_{f_N}(h) = \frac{P_L(h)}{Q_M(h)} = \frac{p_0 + p_1 h^1 + ... + p_l h^l}{q_0 + q_1 h^1 + ... + q_m h^m}. \tag{4.3}$$

Here P_L and Q_M are polynomials of order L and M, where $L + M \leq N$. The coefficients p_i and q_i can be determined using the condition that for a given order N, the series expansion of the Padé approximant at $h = 0$ must be equivalent to $f_N(x)$. While $P[L, M]$ is, by construction, close to the approximated function, the approximant is expected to give more accurate values of $f_\infty(h)$ then the finite series.

For functions with an algebraic divergence at their critical point, like Equation 4.2, critical exponent and point can easily be obtained by [40]

$$\frac{d}{dh} \log[f(x)] = \frac{f'(x)}{f(x)} \propto \frac{z\nu}{(h - h_c)}. \tag{4.4}$$

Applying a Padé extrapolation to 4.4 approximates the critical field strength through the pole location and the critical exponent through the pole residue. This extrapolation technique is referred to as DLogPadé$[L, M]$. The DLogPadé$[L, M]$-method usually yields

28

M poles. To identify the physically relevant ones, prior knowledge of the system is required, since sometimes non-physical poles appear before the physical ones. The corresponding approximants are then called defective. For the DLogPadé method, only cases with $L + M \leq N - 1$ are considered. Here, typically, the best approximants are of the orders $[L, L]$, $[L, L - 1]$ and $[L - 1, L]$

4.2 Square lattice

In this section the results for the square lattice are discussed. At first the series expansion results are presented. The goal of this section is to locate and to investigate the phase transition from the topological phase to the polarized phase, as described in subsection 2.1.4. Since this model is self-dual, it is useful to investigate the system in certain parameter configurations. The most trivial is the Ising-line. Here we only consider a single, parallel field, meaning h_x or h_z. Due to self-duality, only one of the cases has to be investigated. Next, the parallel field case is investigated, where h_x and h_z can be chosen arbitrarily. Here the phase diagram for the parallel field is presented. In the end, the transverse field is turned on. Here we will investigate the multi-critical line, where $h_x = h_z$ and h_y is chosen arbitrary.

4.2.1 Series expansion results

In this section, the bare series results, obtained by applying methods described in chapter 3, are presented. To study the topological phase, small perturbations are considered. To normalize the one particle-gap, $J = \frac{1}{2}$ was set, such that $h_x, h_y, h_z \ll J = \frac{1}{2}$. The ground-state energy, which is symmetric under the exchange of h_x and h_z, can be written down, summarizing certain terms with $S_j = h_x^j + h_z^j$ and $P_{2j} = h_x^j h_z^j$. Calculated up to order 10 it reads:

$$
\begin{aligned}
e_0 = & -1/2 - \frac{1}{2}S_2 - \frac{1}{4}h_y^2 - \frac{15}{8}S_4 - \frac{7}{32}S_2 h_y^2 + \frac{1}{4}P_4 - \frac{13}{192}h_y^4 - \frac{147}{8}S_6 - \frac{371}{128}S_4 h_y^2 \\
& + \frac{113}{32}P_4 S_2 - \frac{1045}{3456}S_2 h_y^4 + \frac{2003}{384}P_4 h_y^2 - \frac{197}{3072}h_y^6 - \frac{18003}{64}S_8 - \frac{1954879}{36864}S_6 h_y^2 \\
& + \frac{6685}{128}P_4 S_4 - \frac{34054175}{3981312}S_4 h_y^4 + \frac{146861}{2304}P_4 S_2 h_y^2 - \frac{15343549}{26542080}S_2 h_y^6 + \frac{20869}{384}P_8 \\
& + \frac{5020085}{497664}P_4 h_y^4 - \frac{163885}{1769472}h_y^8 - \frac{5420775}{1024}S_{10} - \frac{1563459523}{1327104}S_8 h_y^2 + \frac{39524033}{36864}P_4 S_6 \\
& - \frac{1115105409427}{5733089280}S_6 h_y^4 + \frac{10058235445}{7962624}P_4 S_4 h_y^2 - \frac{4219640835497}{191102976000}S_4 h_y^6 \\
& + \frac{5650925}{6912}P_8 S_2 + \frac{20854097563}{143327232}P_4 S_2 h_y^4 - \frac{483890940281}{382205952000}S_2 h_y^8 + \frac{1202498305}{1990656}P_8 h_y^2 \\
& + \frac{1994817656221}{71663616000}P_4 h_y^6 - \frac{186734746441}{1146617856000}h_y^{10}.
\end{aligned}
\tag{4.5}
$$

The one-quasi-particle dispersion $\omega(\mathbf{k})$, with $\mathbf{k}$ being the momentum of the quasi-particle, can be calculated like described in subsection 3.2.2, if the relevant hopping elements t_{ij}

are provided. The expression of $\omega(\mathbf{k})$ reads

$$
\begin{aligned}
\omega(\mathbf{k}) =& 1 - 2h_z(\cos(k_1) + \cos(k_2)) - h_z^2(\cos(2k_1) + 4\cos(k_1)\cos(k_2) + \cos(2k_2) - 2) - h_y^2 \\
&+ \frac{1}{8}h_z\left(\cos(k_1) + \cos(k_2)\right)\cdot \\
&\cdot \left[8h_x^2 - 16h_z^2\left(\cos(2k_1) + 4\cos(k_1)\cos(k_2) + \cos(2k_2) - 3\right) + 11h_y^2\right]
\end{aligned}
\tag{4.6}
$$

in third order which is minimal for $\mathbf{k} = (0,0)$. The single particle gap $\omega(0,0) = \Delta$ has been calculated up to order 9:

$$
\begin{aligned}
\Delta =& 1 - 4h_z - 4h_z^2 - h_y^2 - 12h_z^3 + \frac{11}{4}h_y^2 h_z + 2h_x^2 h_z - 36h_z^4 - 9h_y^2 h_z^2 - \frac{15}{16}h_y^4 + 3h_x^2 h_z^2 \\
&+ 17h_x^2 h_y^2 + 5h_x^4 - 176h_z^5 + \frac{473}{64}h_y^2 h_z^3 + \frac{17}{4}h_y^4 h_z + \frac{83}{4}h_x^2 h_z^3 + \frac{9}{4}h_x^2 h_y^2 h_z + \frac{27}{2}h_x^4 h_z \\
&- \frac{2625}{4}h_z^6 - \frac{7971}{64}h_y^2 h_z^4 - \frac{135619}{3456}h_y^4 h_z^2 - \frac{575}{384}h_y^6 + 63h_x^2 h_z^4 + \frac{1305}{8}h_x^2 h_y^2 h_z^2 \\
&+ \frac{13621}{1152}h_x^2 h_y^4 + 71h_x^4 h_z^2 + \frac{14267}{96}h_x^4 h_y^2 + 92h_x^6 - \frac{14771}{4}h_z^7 - \frac{238621}{1152}h_y^2 h_z^5 \\
&+ \frac{1782929}{20736}h_y^4 h_z^3 + \frac{799973}{110592}h_y^6 h_z + \frac{28633}{64}h_x^2 h_z^5 + \frac{13807}{48}h_x^2 h_y^2 h_z^3 - \frac{3031}{13824}h_x^2 h_y^4 h_z \\
&+ \frac{925}{4}h_x^4 h_z^3 + \frac{1142149}{4608}h_x^4 h_y^2 h_z + \frac{495}{2}h_x^6 h_z - \frac{940739}{64}h_z^8 - \frac{4663837}{1728}h_y^2 h_z^6 \\
&- \frac{1760584999}{1990656}h_y^4 h_z^4 - \frac{1495320677}{19906560}h_y^6 h_z^2 - \frac{26492351}{7962624}h_y^8 + \frac{118029}{64}h_x^2 h_z^6 \\
&+ \frac{5186533}{1728}h_x^2 h_y^2 h_z^4 + \frac{24547709}{165888}h_x^2 h_y^4 h_z^2 + \frac{98263727}{3981312}h_x^2 h_y^6 + \frac{19263}{16}h_x^4 h_z^4 \\
&+ \frac{2199571}{4608}h_x^4 h_y^2 h_z^2 + \frac{3032191}{31104}h_x^4 h_y^4 + \frac{80999}{96}h_x^6 h_z^2 + \frac{7715431}{3072}h_x^6 h_y^2 + \frac{35649}{16}h_x^8 \\
&- \frac{11472297}{128}h_z^9 - \frac{4691521349}{442368}h_y^2 h_z^7 + \frac{538730849}{497664}h_y^4 h_z^5 + \frac{261699729407}{2388787200}h_y^6 h_z^3 \\
&+ \frac{43413180467}{2388787200}h_y^8 h_z + \frac{14650547}{1152}h_x^2 h_z^7 + \frac{2099164741}{165888}h_x^2 h_y^2 h_z^5 - \frac{215708093}{746496}h_x^2 h_y^4 h_z^3 \\
&+ \frac{41328278581}{597196800}h_x^2 h_y^6 h_z + \frac{918461}{144}h_x^4 h_z^5 + \frac{1791338425}{331776}h_x^4 h_y^2 h_z^3 - \frac{1255335587}{11943936}h_x^4 h_y^4 h_z \\
&+ \frac{18372481}{4608}h_x^6 h_z^3 + \frac{2913725647}{663552}h_x^6 h_y^2 h_z + \frac{162525}{32}h_x^8 h_z
\end{aligned}
\tag{4.7}
$$

In this case the particle is a charge, which is moved around the lattice by acting with σ_i^z. Hence, the gap 4.7 possesses uneven orders of h_z. This charge gap is the gap for $h_z \geq h_x$. For $h_z \leq h_x$ one would have to investigate the dispersion of a flux, which can be obtained, by exchanging h_x and h_z in Equation 4.7, due to self-duality. One can easily convince themselves, that both gaps are equal on the self-duality line $h_x = h_z$. Due to lower computational time, in the parallel field case with $h_y = 0$, the gap Δ_p was

calculated up to order 10:

$$
\begin{aligned}
\Delta_p =\ &1 - 4h_z - 4h_z^2 - 12h_z^3 + 2h_x^2 h_z - 36h_z^4 + 3h_x^2 h_z^2 + 5h_x^4 - 176h_z^5 + \frac{83}{4}h_x^2 h_z^3 \\
&+ \frac{27}{2}h_x^4 h_z - \frac{2625}{4}h_z^6 + 63h_x^2 h_z^4 + 71h_x^4 h_z^2 + 92h_x^6 - \frac{14771}{4}h_z^7 + \frac{28633}{64}h_x^2 h_z^5 + \frac{925}{4}h_x^4 h_z^3 \\
&+ \frac{495}{2}h_x^6 h_z - \frac{940739}{64}h_z^8 + \frac{118029}{64}h_x^2 h_z^6 + \frac{19263}{16}h_x^4 h_z^4 + \frac{80999}{96}h_x^6 h_z^2 + \frac{35649}{16}h_x^8 \\
&- \frac{11472297}{128}h_z^9 + \frac{14650547}{1152}h_x^2 h_z^7 + \frac{918461}{144}h_x^4 h_z^5 + \frac{18372481}{4608}h_x^6 h_z^3 + \frac{162525}{32}h_x^8 h_z \\
&- \frac{287258435}{768}h_z^{10} + \frac{96935975}{1728}h_x^2 h_z^8 + \frac{107740069}{3456}h_x^4 h_z^6 + \frac{21893537}{1536}h_x^6 h_z^4 \\
&+ \frac{43593271}{3072}h_x^8 h_z^2 + \frac{1873147}{32}h_x^{10} \tag{4.8}
\end{aligned}
$$

The same considerations like before hold true.

4.2.2 Ising-lines

Due to the exact mapping of the toric code in a single, parallel field onto the 3d-transverse field Ising model on the square lattice in the flux-free (charge-free) sector, as seen in subsection 2.1.4, the values for the critical field strength h_c, at which the system transitions from the topological phase to the polarized one, and the critical exponent νz are known. Converted to our parameters, the critical field strength is given by $h_c = 0.164235(11)$ [33], while the 3D-Ising universality class is known to have $z = 1$ and $\nu = 0.6301(4)$ [41, 42] at the phase transition . By comparing our results to these critical parameters, we can estimate the reliability of our extrapolations.

The results of the DLogPadé extrapolation are shown in Table 4.1. Our results for the critical field strength in z-direction coincide with the well-studied value of h_c. As mentioned in section 4.1, the best results lie on or near the diagonal, meaning $L = M$ or $L = M \pm 1$. Our results for the critical exponent, while still near, overestimate the expected νz, which is typical for DLogPadé extrapolations, since they ignore subleading corrections to the critical behaviour [43].

$L\backslash M$	1	2	3	4	5	6	7	8
1	0.162162	0.164715	0.165169	0.164830	0.164564	0.164501	0.164470	0.164415
2	0.168182	0.165165	0.164986	0.162457	0.164484	0.164441	0.164540*	–
3	0.162242	0.164836	0.161615	0.164601	0.164457	0.164502*	–	–
4	0.166905	0.164563	0.164477	0.164453	0.164312	–	–	–
5	0.162267	0.164496	0.164444	0.164489*	–	–	–	–
6	0.166614	0.164467	0.164532*	–	–	–	–	–
7	0.162424	0.164413	–	–	–	–	–	–
8	0.166252	–	–	–	–	–	–	–

(a)

$L\backslash M$	1	2	3	4	5	6	7	8
1	0.631118	0.655552	0.660874	0.655370	0.650054	0.648568	0.647735	0.646001
2	0.704042	0.660812	0.658256	0.550358	0.648092	0.646681	0.649293*	–
3	0.609726	0.655478	0.493062	0.651400	0.647259	0.648492*	–	–
4	0.702536	0.650010	0.647872	0.647149	0.641509	–	–	–
5	0.593237	0.648412	0.646805	0.648154*	–	–	–	–
6	0.713847	0.647609	0.649089*	–	–	–	–	–
7	0.582260	0.645906	–	–	–	–	–	–
8	0.718076	–	–	–	–	–	–	–

(b)

Table 4.1: Results from the DLogPadé$[L, M]$ extrapolations for a single parallel field. (a) Results for the critical field strength h_c. (b) Results for the critical exponent νz. Values marked with an asterisk denote defective extrapolations

4.2.3 Parallel fields

After confirming the results for the Ising-line, the next step is to investigate the critical behaviour along the self-duality line and then for a more general parallel field, where $h_x \neq h_z$. Since the field now consists of multiple parameters, we will represent it as a vector $\mathbf{h} = (h_x, h_y, h_z)$. For the parallel case, we have $h_y = 0$, thus $\mathbf{h} = h(\sin(\phi), 0, \cos(\phi))$. The Ising-line can be obtained by choosing $\phi = 0$, while $\phi = \frac{\pi}{4}$ describes the self-duality line. Using the particle symmetry, critical field strengths and exponents only have to be calculated for $\phi \in [0, \frac{\pi}{4}]$. The results for the multicritical point with $\phi = \frac{\pi}{4}$ can be seen in Table 4.2. There, (a) shows the position of the multicritical point, meaning the value of $h_c = |\mathbf{h}|$, at which the system experiences a phase transition along the self-duality line. Here the value we extrapolated for h_c is larger than for the Ising line. For the multicritical point, we find the critical exponent $\nu z \simeq 0.69$, which is considerably larger than the critical exponent for the Ising line. This calculation can be done for every angle ϕ.

In Figure 4.2, the different approximants are plotted for an increasing angle ϕ. While they largely converge, some approximants have kinks or other divergences, at which the extrapolation failed locally. These local deviations can be disregarded, since other approximations still converge. Using these values, one can construct a phase diagram

$L\backslash M$	1	2	3	4	5	6	7	8
1	0.239022	0.232429*	0.241976	0.240962	0.241057	0.240892	0.240999	0.240927
2	0.246100	0.241872	0.241210	0.241047	0.240997	0.240956	0.240956	–
3	0.235859	0.241010	0.241042	0.240569	0.240950	0.240956	–	–
4	0.246456	0.241043	0.241016	0.240946	0.240957	–	–	–
5	0.235639	0.240903	0.240955	0.240956	–	–	–	–
6	0.246113	0.240988	0.240956	–	–	–	–	–
7	0.236273	0.240935	–	–	–	–	–	–
8	0.245294	–	–	–	–	–	–	–

(a)

$L\backslash M$	1	2	3	4	5	6	7	8
1	0.685578	0.666934*	0.706586	0.695017	0.696389	0.693522	0.695689	0.694034
2	0.748313	0.705431	0.698410	0.696226	0.695461	0.694745	0.694752	–
3	0.631305	0.695680	0.696132	0.683557	0.694610	0.694752	–	–
4	0.786464	0.696156	0.695757	0.694532	0.694782	–	–	–
5	0.600785	0.693724	0.694728	0.694738	–	–	–	–
6	0.814585	0.695449	0.694738	–	–	–	–	–
7	0.587717	0.694235	–	–	–	–	–	–
8	0.823430	–	–	–	–	–	–	–

(b)

Table 4.2: Results from the DLogPadé$[L, M]$ extrapolations for the duality line with $h_x = h_z$. (a) Results for the critical field strength h_c. (b) Results for the critical exponent νz. Values marked with an asterisk denote defective extrapolations.

for the toric code in a parallel field, as seen in Figure 4.3. Our phase diagram is in good agreement with previous results, like the ones obtained by the continuous-time quantum Monte Carlo method in [19], by analytical calculations in [18] or by series expansions in order 9 in [25]. The first-order phase transition, that extends from the multicritical point along the self-duality line (see Figure 2.8) is missing, since it is not possible to obtain this first-order phase transition by the perturbative series approach in the topological phase. Now, we evaluate the changes to the critical exponent νz along the phase transition. By comparing the values at the Ising point in Table 4.1 and at the multicritical point in Table 4.2, an increase of the critical exponent can be noticed. The precise course of the critical exponent can be seen in Figure 4.4. Here we can see, that, apart form non-physical divergences, the critical value remains almost the same for an increasing angle ϕ, which indicates, that the universality class of the system is still similar to the 3D-Ising model. Only for ϕ near $\frac{\pi}{4}$, meaning the multicritical point, the critical exponent grows, which is evidence for a different universality class. A possible reason for this might be, that on the multicritical point both charges and fluxes condense simultaneously. In that case, the mutual exchange statistics would be of importance.
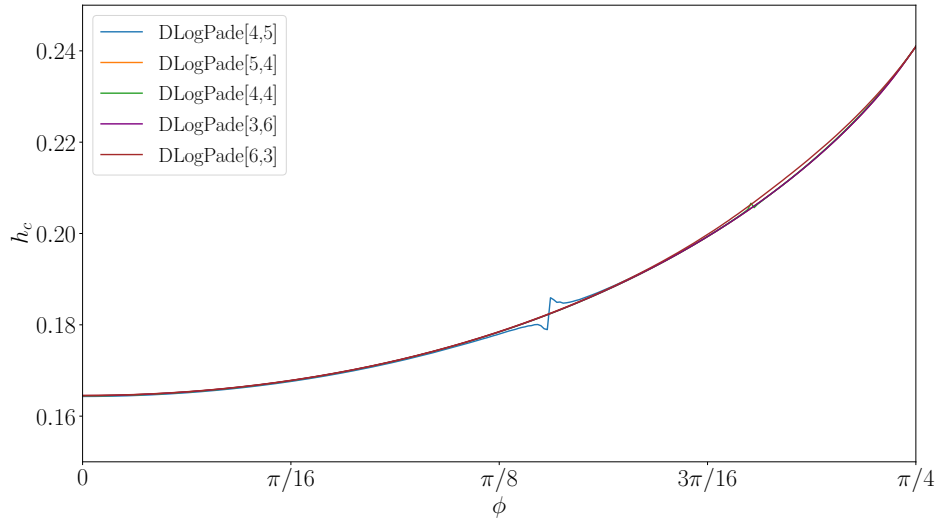
Figure 4.2: Selected DLogPadé extrapolations for the critical field strength in dependence of the angle ϕ. Single approximants fail at certain values, like DLogPadé$[4,5]$ at around $\phi = \frac{\pi}{8}$. For a field $h < h_c$ at a certain angle ϕ, the system realizes the topological phase, while for $h > h_c$ the system realizes a polarized one.
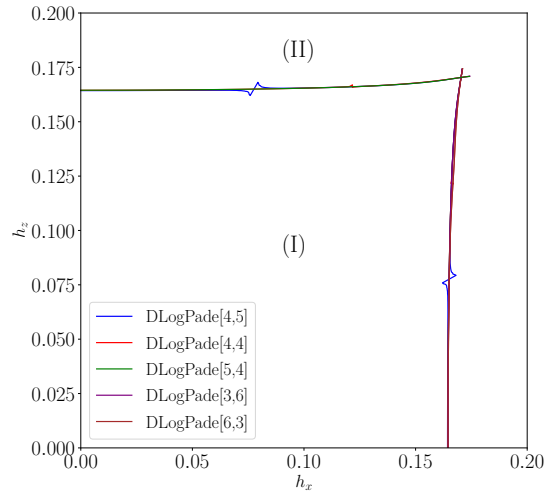
Figure 4.3: Phase diagram of the toric code on a square lattice in a parallel field. The topological phase, marked by (I), is separated by a second order phase transition, indicated by lines, from the polarized phase, marked by (II). This phase diagram depicts only the second-order phase transitions, obtained by DLogPadé approximation, while the first-order phase-transition line outside the topological phase seen in Figure 2.8 is not shown.
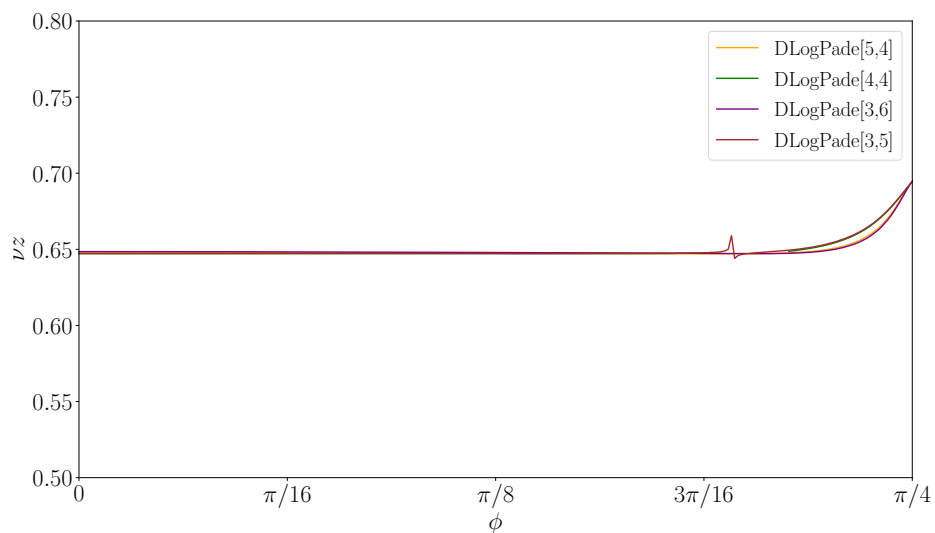
Figure 4.4: Critical exponent νz along the phase transition, parameterized by ϕ. Some extrapolations deviate from the rest, like the DLogPadé[4,5]-extrapolation for $\phi < \frac{3\pi}{16}$, or the DLogPadé[4,4] and DLogPadé[5,5]-extrapolation at around $\frac{3\pi}{16}$. These approximants can be disregarded as these have non-physical divergences. Since the DLogPadé[4,5]-approximant already diverges strongly form the other approximants on the Ising line, it can also be ignored.

4.2.4 Parallel and transverse field

After investigating the case, in which the field is a combination of parallel ones, it is time to consider arbitrary field directions. Here Kamfor, Schmidt et al. [21, 25] used infinite projected entangled-pair states (iPEPS)[44] and pCUT. There, it has been shown, that the toric code undergoes a second- or first-order phase transition form the topological to the polarized phase, depending on the field orientation. In this subsection we will again consider the field-vector $\mathbf{h} = (h_x, h_y, h_z) = h(\sin(\phi)\cos(\theta), \sin(\theta), \cos(\phi)\cos(\theta))$. A sketch of this vector can be seen in Figure 4.5. To investigate the behaviour of the system for a finite transverse field h_y, the angle θ is introduced. For $\theta = 0$, we recover the parallel field case. For θ near $\frac{\pi}{2}$ a first-order phase transition is expected [21]. This coincides well with the first-order phase transition for the Xu-Moore-model [17], mentioned in subsection 2.1.4. For θ near 0, a second-order phase transition is expected. In this chapter we will investigate the critical behaviour in dependence of θ for the cases $\phi = 0$, $\phi = \frac{\pi}{8}$ and finally $\phi = \frac{\pi}{4}$. The last case is of special interest, since it describes, how the multicritical point behaves as a function of h_y.
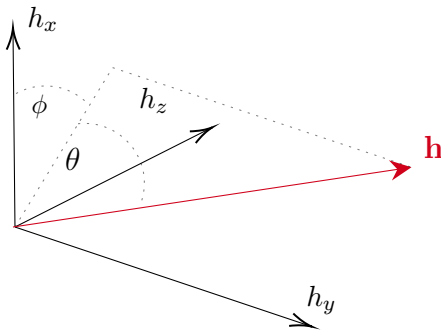

Figure 4.5: Sketch of the vector $\mathbf{h} = h(\sin(\phi)\cos(\theta), \sin(\theta), \cos(\phi)\cos(\theta))$. $\mathbf{h}$ is colored red.

The development of the critical field strength h_c for the cases with $\phi = 0$ and $\phi = \frac{\pi}{8}$ is very similar for increasing θ. The extrapolated critical field strength values h_c are both depicted in Figure 4.6. Most extrapolations converge. In both figures, the vertical black lines indicate, at which values of θ the DLogPadé approximants are no longer valid, since the iPEPS-method indicates a first-order phase transition in this parameter domain [21], that is not detected by our extrapolation method. The corresponding values have been taken from the PhD thesis of Michael Kamfor [25]. There also a detailed approach to the iPEPS method can be found. As expected, approximants in Figure 4.6 begin to diverge beyond these values, since their behaviour is no longer physical.

We now consider the critical exponent for the discussed phase transitions. The course of the critical exponents for the cases $\phi = 0$ and $\phi = \frac{\pi}{8}$ can be seen in Figure 4.7, plotted against the angle θ. The vertical black lines again indicate the end of the validity of our extrapolations. The course of the critical exponent in both cases look very similar. For almost the whole parameter space of θ, the exponent stay constant at $\nu z \simeq 0.65$, which corresponds to the critical exponent on the Ising line (see Table 4.1). This indicates,
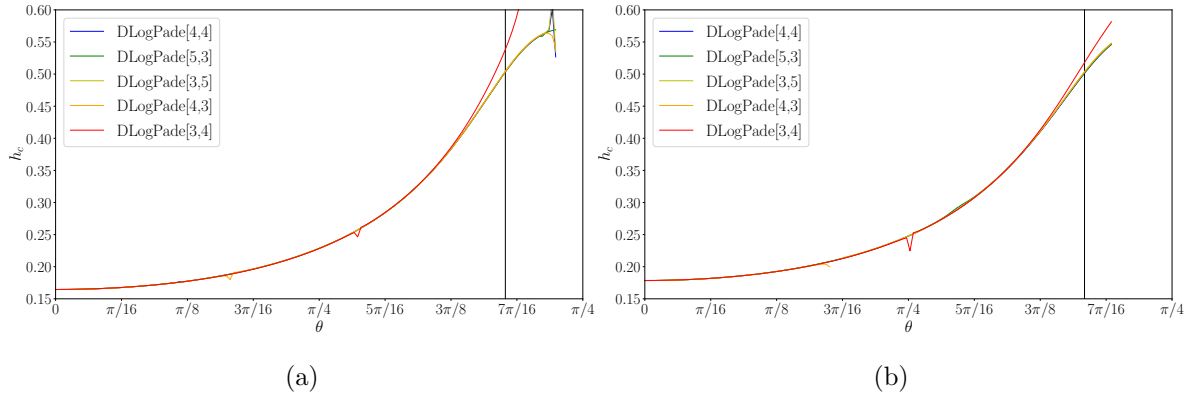
Figure 4.6: The course of the critical field strength for increasing θ for $\phi = 0$ in (a) and $\phi = \frac{\pi}{8}$ in (b). The vertical black lines indicates the end of the validity of our extrapolations, since first-order phase transitions were found beyond these lines in [25]. They lie at $\theta = 1.34$ for (a) and $\theta = 1.316$ for (b).

that the system remains in the 3d-Ising universality class. Only near the first-order phase transition domain, the critical exponents begin to diverge. By inspecting the order of the approximants, one can recognize, that this decreasing behaviour near the first-order phase transition domain is reducing in higher orders.

Now it is time to investigate the behaviour of the multicritical point for a finite transverse field. The course of h_c is shown in Figure 4.8. Again, the approximants begin to diverge in the first-order phase transition domain, marked by the vertical line. Here the critical exponents are of special interest. These are shown in Figure 4.9. One can see, that the exponent grows from $\nu z = 0.69$ at $\theta = 0$ to a value closer to $\nu z = 1$ at $\theta = 1.082$, which corresponds to $h_y = 0.46$. Since this is a huge increase, it is reasonable to suggest, that this behaviour reveals a new universality class. Earlier studies [21] used the same methods of DLogPadé approximations and pCUT to calculate these up to order 8. In this case, the exponent converged to $\nu z \simeq 1$. We were able to confirm, that this behaviour is still present in order 9. Figure 4.10 shows the extrapolated critical exponent νz at the domain threshold $\theta = 1.082$. The course of these dLogPadé families suggests, that this behaviour does not stem from extrapolation errors, but is indeed the realisation of a new universality class. New calculations however did not yield any insight how this change happens (for example a sharper incline at the domain threshold).
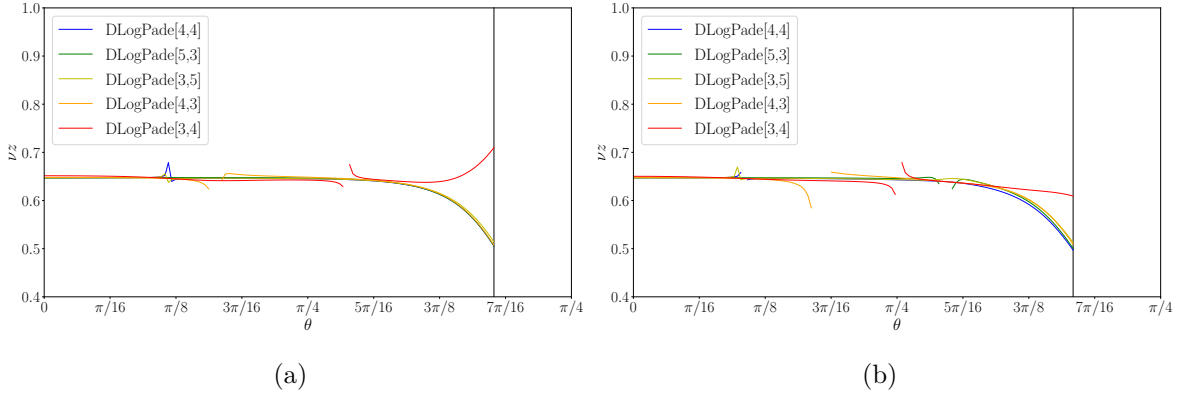
(a)

(b)

Figure 4.7: The course of the critical exponent νz for increasing θ for $\phi = 0$ in (a) and $\phi = \frac{\pi}{8}$ in (b). The vertical black lines indicate the end of the validity of our extrapolations, since first-order phase transitions were found beyond these lines in [25]. They lie at $\theta = 1.34$ for (a) and $\theta = 1.316$ for (b). In both cases some approximants have non-physical divergences for $\frac{\pi}{8} < \theta < \frac{\pi}{4}$. Since the other approximants converge at those values, these divergences can be ignored, since they are non-physical.
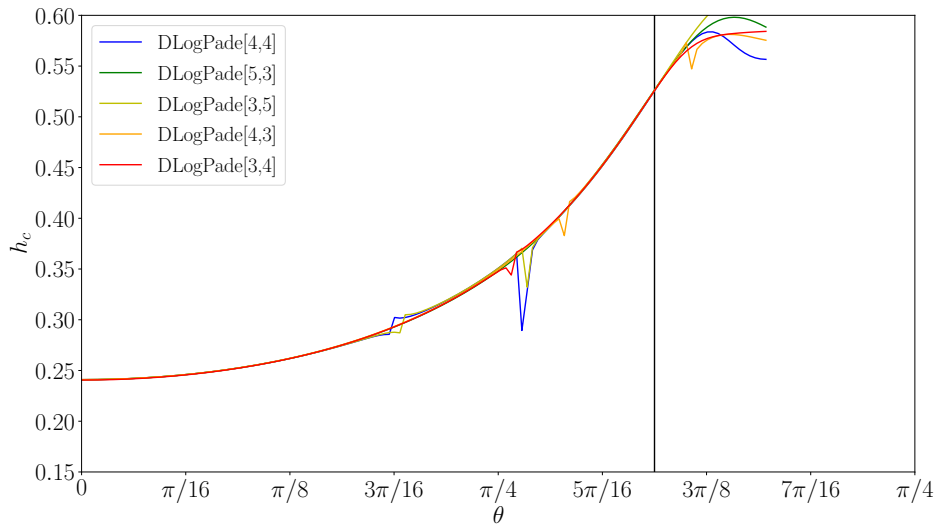
Figure 4.8: Approximants for the critical field strength h_c for increasing θ for $\phi = \frac{\pi}{4}$. The vertical black line indicates the end of the validity of our extrapolations, since first-order phase transitions were found beyond this line in [25], and lies at $\theta = 1.082$. Beyond that line the approximants begin to diverge, just as in Figure 4.6.

39
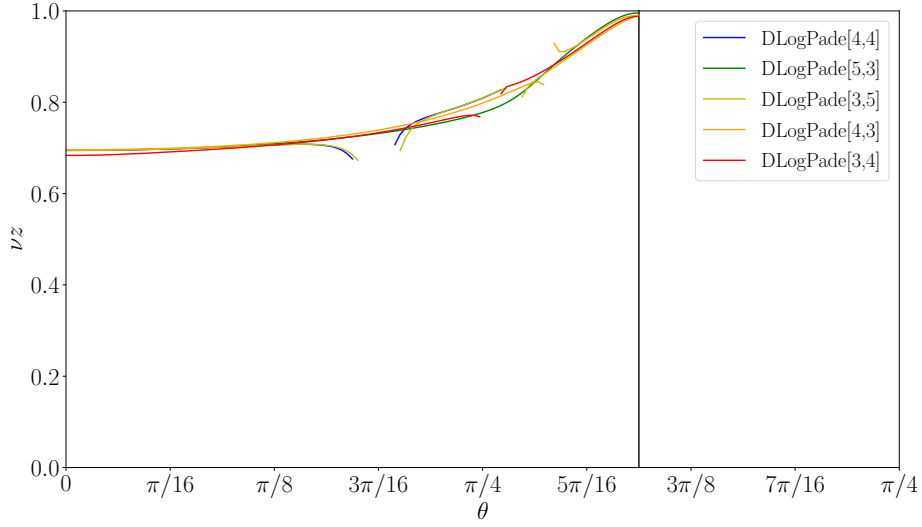
Figure 4.9: The course of the critical field strength for increasing θ for $\phi = \frac{\pi}{4}$. The vertical black lines indicates the end of the validity of our extrapolations, since first-order phase transitions were found beyond this line in [25], and lies at $\theta = 1.082$. Spurious poles emerge in the area of $\frac{\pi}{4} < \theta < \frac{5\pi}{16}$ and can be considered non-physical.
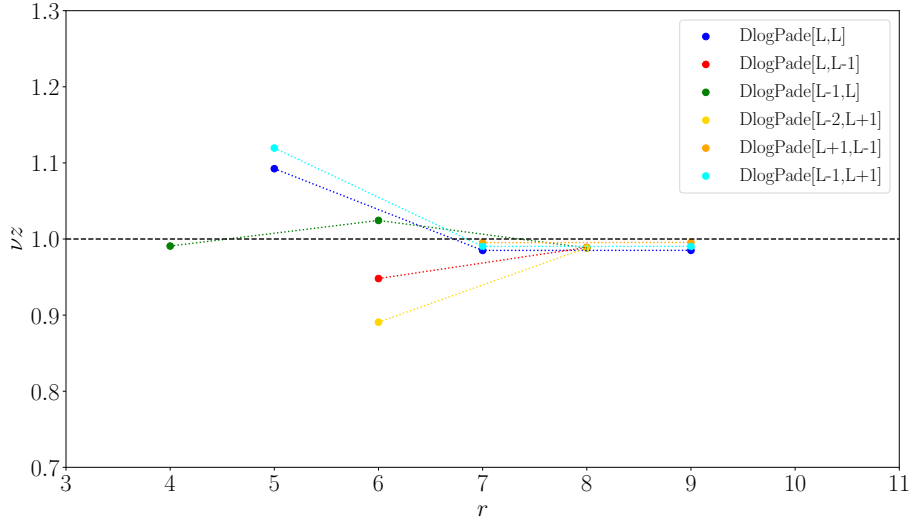
Figure 4.10: Critical exponents νz of the end of the multicritical line with $\theta = 1.082$ with multiple DLogPadé families. For the extrapolation order r one has $L = \frac{r - (r \mod 2)}{2}$. The black, vertical line marks $\nu z = 1$

4.3   Honeycomb lattice

In this section the results for the honeycomb lattice are discussed. First, we present the series expansion results. The phase transitions will be located and investigated. We again check our extrapolation methods by considering the Ising lines. This model is no longer self-dual, like the toric code on a square lattice, and realizes geometric frustration, depending on the sign of h_x. Hence we can not use as many symmetries, as in previous chapter. After calculating the phase-diagram for a parallel field, the system's behaviour in a general magnetic field is investigated.

4.3.1   Series expansion results

The bare series results, obtained by applying the methods described in chapter 3, are presented here. To study the topological phase, small perturbations in h are considered. To normalize the one particle-gap, $J = \frac{1}{2}$ was set, such that $h_x, h_y, h_z \ll J = \frac{1}{2}$. Calculated up to order 9 the ground-state energy per site reads:

$$
\begin{aligned}
e_0 = &-\frac{1}{2} - \frac{1}{2}h_x^2 - \frac{1}{2}h_z^2 - \frac{1}{4}h_y^2 - h_x^3 - \frac{29}{8}h_x^4 - \frac{3}{8}h_z^4 - \frac{5}{64}h_y^4 + \frac{1}{4}h_x^2 h_z^2 - \frac{13}{32}h_x^2 h_y^2 \\
&- \frac{1}{8}h_z^2 h_y^2 + \frac{117}{4}h_x^5 - \frac{123}{2}h_x^3 h_z^2 - \frac{1307}{64}h_x^3 h_y^2 + \frac{21}{64}h_x h_z^2 h_y^2 - \frac{1157}{8}h_x^6 - \frac{61}{16}h_z^6 \\
&- \frac{23257}{276480}h_y^6 + \frac{219}{32}h_x^4 h_z^2 - \frac{8285}{768}h_x^4 h_y^2 + \frac{5}{8}h_x^2 h_z^4 - \frac{289}{384}h_x^2 h_y^4 + \frac{57}{128}h_x^2 h_z^2 h_y^2 \\
&- \frac{295}{768}h_z^4 h_y^2 - \frac{85}{432}h_z^2 h_y^4 - \frac{35957}{16}h_x^7 - \frac{38715}{64}h_x^5 h_z^2 - \frac{256565}{576}h_x^5 h_y^2 - \frac{1015}{64}h_x^3 h_z^4 \\
&- \frac{36037}{512}h_x^3 h_z^2 h_y^2 - \frac{1205675}{27648}h_x^3 h_y^4 + \frac{70073}{4608}h_x h_z^4 h_y^2 + \frac{40153}{13824}h_x h_z^2 h_y^4 - \frac{621271}{128}h_x^8 \\
&- \frac{2401}{128}h_z^8 - \frac{508809373}{3981312000}h_y^8 + \frac{170851}{768}h_x^6 h_z^2 - \frac{67005631}{110592}h_x^6 h_y^2 + \frac{2467}{128}h_x^4 h_z^4 \\
&+ \frac{251825}{6912}h_x^4 h_z^2 h_y^2 - \frac{2214061}{73728}h_x^4 h_y^4 + \frac{8489}{768}h_x^2 h_z^6 + \frac{3096779}{110592}h_x^2 h_z^4 h_y^2 \\
&- \frac{37740013}{4976640}h_x^2 h_z^2 h_y^4 - \frac{1541612851}{995328000}h_x^2 h_y^6 - \frac{19075}{3072}h_z^6 h_y^2 - \frac{447433}{497664}h_z^4 h_y^4 \\
&- \frac{431610577}{995328000}h_z^2 h_y^6 - \frac{2556539}{64}h_x^9 + \frac{376405}{576}h_x^7 h_z^2 - \frac{173127763}{24576}h_x^7 h_y^2 + \frac{146115}{512}h_x^5 h_z^4 \\
&- \frac{23772923623}{47775744}h_x^5 h_y^4 - \frac{11053051}{221184}h_x^5 h_z^2 h_y^2 - \frac{77977}{4608}h_x^3 h_z^6 + \frac{7153981}{41472}h_x^3 h_z^4 h_y^2 \\
&- \frac{2741829491}{47775744}h_x^3 h_z^2 h_y^4 - \frac{174404206741}{11943936000}h_x^3 h_y^6 + \frac{27147607}{442368}h_x h_z^6 h_y^2 + \frac{204101125}{5971968}h_x h_z^4 h_y^4 \\
&+ \frac{20658157247}{11943936000}h_x h_z^2 h_y^6 .
\end{aligned}
\tag{4.9}
$$

Unlike the ground-state energy 4.5, the series for the honeycomb lattice contains odd powers of h_x, since here loops can consist of an odd number of plaquette-sites. Since

this model is no longer self-dual, dispersion relations for fluxes and charges have to be considered separately. First we will consider charges, or star-particles, that live on a bipartite, hexagonal lattice. This particle-type is moved or created, by perturbing the lattice with σ^z-perturbations. By calculating the hopping elements, as described in subsection 3.2.2, one can calculate the dispersion:

$$
\begin{aligned}
\omega_c(\mathbf{k}) =& 1 + h_z \left[4\cos(k_1) - 2h_x^2\cos(k_1) - \frac{5}{2}h_y^2\cos(k_1) + 2\cos(k_2) - h_x^2\cos(k_2) - \frac{5}{4}h_y^2\cos(k_2) \right] \\
& - \frac{3}{2}h_y^2 - 6h_x^3 - \frac{17}{4}h_x h_y^2\cos(2k_1) - \frac{17}{4}h_x h_y^2\cos(k_1 - k_2) - \frac{17}{4}h_x h_y^2\cos(k_1 + k_2) \\
& + h_z^2 \left[3 - 2\cos(2k_1) - 2\cos(k_1 - k_2) - 2\cos(k_1 + k_2) \right] \\
& + h_z^3 \left[-4\cos(k_1) + 2\cos(3k_1) + \cos(k_1 - 2k_2) + \right. \\
& \left. \qquad\qquad 3\cos(2k_1 - k_2) + 3\cos(2k_1 + k_2) + \cos(k_1 + 2k_2) \right].
\end{aligned}
$$
(4.10)

Here the minimum is always found at $\mathbf{k} = (0,0)$. The one-charge gap up to order 7 then reads:

$$
\begin{aligned}
\Delta_c =& 1 - 3h_z - \frac{3}{2}h_z^2 - \frac{3}{4}h_y^2 - 3h_z^3 - \frac{15}{8}h_y^2 h_z - \frac{51}{8}h_x h_y^2 + \frac{3}{2}h_x^2 h_z + 3h_x^3 - \frac{81}{8}h_z^4 \\
& - \frac{141}{32}h_y^2 h_z^2 - \frac{75}{64}h_y^4 - \frac{129}{16}h_x h_y^2 h_z + \frac{3}{4}h_x^2 h_z^2 + \frac{171}{32}h_x^2 h_y^2 + 15h_x^4 - \frac{57}{2}h_z^5 + \frac{1131}{128}h_y^2 h_z^3 \\
& - \frac{229}{48}h_y^4 h_z - \frac{6573}{128}h_x h_y^2 h_z^2 + \frac{1423}{192}h_x h_y^4 + \frac{51}{8}h_x^2 h_z^3 + \frac{3087}{64}h_x^2 h_y^2 h_z + \frac{123}{8}h_x^3 h_z^2 \\
& + \frac{6465}{128}h_x^3 h_y^2 + \frac{141}{8}h_x^4 h_z + 102h_x^5 - \frac{1011}{16}h_z^6 - \frac{18509}{512}h_y^2 h_z^4 - \frac{41183}{2304}h_y^4 h_z^2 - \frac{29961}{10240}h_y^6 \\
& - \frac{537}{16}h_x h_y^2 h_z^3 - \frac{1857}{128}h_x h_y^4 h_z + \frac{507}{32}h_x^2 h_z^4 - \frac{24237}{256}h_x^2 h_y^2 h_z^2 + \frac{9623}{1152}h_x^2 h_y^4 + \frac{117}{16}h_x^3 h_z^3 \\
& + \frac{603}{16}h_x^3 h_y^2 h_z - \frac{69}{32}h_x^4 h_z^2 + \frac{64839}{256}h_x^4 h_y^2 + 72h_x^5 h_z + \frac{2961}{4}h_x^6 - \frac{8529}{32}h_z^7 \\
& + \frac{28763}{1024}h_y^2 h_z^5 + \frac{305539}{9216}h_y^4 h_z^3 - \frac{29441687}{1843200}h_y^6 h_z - \frac{554771}{1536}h_x h_y^2 h_z^4 - \frac{2751173}{27648}h_x h_y^4 h_z^2 \\
& - \frac{708773}{61440}h_x h_y^6 + \frac{10251}{128}h_x^2 h_z^5 + \frac{1935065}{3072}h_x^2 h_y^2 h_z^3 + \frac{24717}{1024}h_x^2 h_y^4 h_z + \frac{21681}{128}h_x^3 h_z^4 \\
& + \frac{739141}{1536}h_x^3 h_y^2 h_z^2 + \frac{13019}{128}h_x^3 h_y^4 + \frac{15423}{64}h_x^4 h_z^3 + \frac{1659521}{3072}h_x^4 h_y^2 h_z + \frac{12801}{128}h_x^5 h_z^2 \\
& + \frac{2630047}{1536}h_x^5 h_y^2 + 543h_x^6 h_z + 5547h_x^7.
\end{aligned}
$$
(4.11)

As discussed in subsection 2.1.4, fluxes, or plaquette-excitations move on a triangular lattice. The corresponding dispersion reads

$$
\begin{aligned}
\omega_f(\mathbf{k}) = 1 + h_x & \Big[2\cos(k_1) - h_z^2\cos(k_1) - \frac{13}{8}h_y^2\cos(k_1) + 2\cos(k_1 - k_2) - h_z^2\cos(k_1 - k_2) \\
& - \frac{13}{8}h_y^2\cos(k_1 - k_2) + 2\cos(k_2) - h_z^2\cos(k_2) - \frac{13}{8}h_y^2\cos(k_2) \Big] \\
+ h_x^2 & \Big[3 - 2\cos(k_1) - \cos(2k_1) - 2\cos(k_1 - 2k_2) - \cos(2k_1 - 2k_2) \\
& - 2\cos(k_1 - k_2) - 2\cos(2k_1 - k_2) - 2\cos(k_2) - \cos(2k_2) - 2\cos(k_1 + k_2) \Big] \\
- \frac{3}{2}h_y^2 &
\end{aligned}
\tag{4.12}
$$

up to second order. For arbitrary orders it can be shown, that this dispersion takes its minimal value at $\mathbf{k} = (0,0)$, if $h_x > 0$. In this case, the dual model in the charge-free sector would be the ferromagnetically coupled transverse field Ising model discussed earlier. For $h_x < 0$, $\omega(\mathbf{k})$ reaches its minimum at $\mathbf{k} = (\pm\frac{2}{3}\pi, \mp\frac{2}{3}\pi)$. Here a mapping to the antiferromagnetic transverse field Ising model is possible in the charge-free sector. For $h_x > 0$, the gap has been calculated up to order 7:

$$
\begin{aligned}
\Delta_{f,h_x^+} = & 1 - 6h_x - \frac{3}{2}h_z^2 - 12h_x^2 + \frac{39}{8}h_x h_z^2 + 3h_x h_y^2 - 42h_x^3 - \frac{27}{32}h_z^4 - \frac{45}{16}h_y^2 h_z^2 \\
& - \frac{237}{8}h_x^2 h_z^2 + \frac{21}{2}h_x^2 h_y^2 - 252h_x^4 + \frac{23}{8}h_x h_z^4 + \frac{2331}{64}h_x h_y^2 h_z^2 + \frac{51}{4}h_x h_y^4 - \frac{4179}{128}h_x^3 h_z^2 \\
& + \frac{543}{8}h_x^3 h_y^2 - \frac{3153}{2}h_x^5 - \frac{63091}{46080}h_z^6 - \frac{8779}{1152}h_y^2 h_z^4 + \frac{36099}{256}h_y^4 h_z^2 + \frac{63}{2}h_y^6 \\
& - \frac{63437}{2304}h_x^2 h_z^4 - \frac{10725}{64}h_x^2 h_y^2 h_z^2 + \frac{315}{16}h_x^2 h_y^4 - \frac{265363}{256}h_x^4 h_z^2 + \frac{3795}{8}h_x^4 h_y^2 - \frac{44379}{4}h_x^6 \\
& + \frac{833057}{115200}h_x h_z^6 - \frac{229877}{1152}h_x h_y^2 h_z^4 - \frac{112649}{512}h_x h_y^4 h_z^2 + \frac{345}{4}h_x h_y^6 - \frac{7582669}{27648}h_x^3 h_z^4 \\
& + \frac{510259}{512}h_x^3 h_y^2 h_z^2 + \frac{18687}{64}h_x^3 h_y^4 - \frac{9540703}{1536}h_x^5 h_z^2 + \frac{500301}{128}h_x^5 h_y^2 - \frac{2545713}{32}h_x^7
\end{aligned}
\tag{4.13}
$$

For $h_x < 0$, the gap up to order 7 reads:

$$
\begin{aligned}
\Delta_{f,h_x^-} =\ &1 + 3h_x - \frac{3}{2}h_z^2 + \frac{3}{2}h_x^2 - \frac{39}{16}h_x h_z^2 - \frac{3}{2}h_x h_y^2 + \frac{15}{2}h_x^3 - \frac{27}{32}h_z^4 - \frac{135}{32}h_y^2 h_z^2 \\
&- \frac{273}{32}h_x^2 h_z^2 - 3h_x^2 h_y^2 + \frac{243}{8}h_x^4 - \frac{23}{16}h_x h_z^4 - \frac{1845}{128}h_x h_y^2 h_z^2 - \frac{51}{8}h_x h_y^4 - \frac{3693}{128}h_x^3 h_z^2 \\
&- \frac{219}{16}h_x^3 h_y^2 + \frac{1671}{8}h_x^5 - \frac{63091}{46080}h_z^6 - \frac{42835}{4608}h_y^2 h_z^4 - \frac{3819}{512}h_y^4 h_z^2 + \frac{63}{2}h_y^6 \\
&- \frac{124385}{9216}h_x^2 h_z^4 - \frac{21435}{256}h_x^2 h_y^2 h_z^2 - \frac{423}{32}h_x^2 h_y^4 - \frac{64715}{512}h_x^4 h_z^2 - \frac{2217}{32}h_x^4 h_y^2 + \frac{22275}{16}h_x^6 \\
&- \frac{833057}{230400}h_x h_z^6 - \frac{343267}{9216}h_x h_y^2 h_z^4 - \frac{115641}{2048}h_x h_y^4 h_z^2 - \frac{345}{8}h_x h_y^6 - \frac{1991593}{27648}h_x^3 h_z^4 \\
&- \frac{498235}{1024}h_x^3 h_y^2 h_z^2 - \frac{11721}{128}h_x^3 h_y^4 - \frac{4637225}{12288}h_x^5 h_z^2 - \frac{70533}{128}h_x^5 h_y^2 + \frac{162855}{16}h_x^7.
\end{aligned}
$$
$$(4.14)$$

With these one-particle gaps, we can detect the breakdown of the topological phase.

4.3.2 Ising-lines

Just as for the square lattice, we will check the validity of our extrapolations, by comparing them to already known values for the Ising lines ($h_x = 0$ or $h_z = 0$). First, we will compare our results for $h_x = 0$ with values for the transverse field Ising model on a hexagonal lattice, since here a mapping can be found for the flux-free sector. Due to the bipartitness of the hexagonal lattice, only $h_z > 0$ has to be considered, since the same behaviour is expected for $h_z < 0$. In [33], the critical behaviour of the hexagonal transverse field Ising model was investigated. There, rescaled to our model, $h_c = 0.234467(5)$ was found. Since the hexagonal transverse field Ising model belongs again to the 3D-Ising universality class, $\nu = 0.6301(4)$ still holds [41, 42]. The results of our extrapolations are listed in Table 4.3. Here, (a) shows the results for the critical field strength h_c, at which the system transitions out of the topological phase, while (b) shows the corresponding critical exponent νz. Our results for h_c yield a rather precise estimate, while our results for νz fluctuate strongly. To suppress these fluctuations, higher orders would be necessary. Nonetheless, DLogPadé approximations for $[L, M] = [2, 4]$ and [3, 3] seem relatively accurate estimates, keeping in mind, that some overestimation is expected [43].

Now we consider the case for $h_z = 0$ and $h_x > 0$. The dual model for the charge-free sector is the ferromagnetically coupled transverse field Ising model on a triangular lattice. For the ferromagnetic case, the system is still in the 3D-Ising universality class, where, converted to our units, $h_c = 0.104863(2)$ has been found in [33], using a cluster Monte Carlo method. The extrapolation values are listed in Table 4.4. The extrapolated values for h_c, as seen in 4.4a, converge nicely and agree with the expected value. The corresponding critical exponents are listed in 4.4b. Their values also converge and are

$L \backslash M$	1	2	3	4	5
1	0.242424	0.257820	0.232008	0.230801*	0.236794
2	0.229167*	0.231482	0.237150*	0.234988	–
3	0.231978	0.227928	0.234899	–	–
4	0.241725*	0.233466	–	–	–
5	0.233466	–	–	–	–

(a)

$L \backslash M$	1	2	3	4	5
1	0.705234	0.751342*	0.625583	0.614497*	0.685498
2	0.595744*	0.619091	0.682434*	0.656598	–
3	0.625514	0.587579*	0.655345	–	–
4	0.768451	0.692324	–	–	–
5	0.623773	–	–	–	–

(b)

Table 4.3: Results from the DLogPadé$[L, M]$ extrapolations for the single parallel field h_z. (a) Results for the critical field strength h_c. (b) Results for the critical exponent νz. Values marked with an asterisk denote defective extrapolations

in good agreement with the expected value, considering a slight overestimation of the DLogPadé extrapolation.

In the charge-free sector for $h_z = 0$ and $h_x < 0$ the dual model describes the antiferro-magnetic transverse field Ising model on a triangular lattice. Here the model realizes a phase transition inside the 3D-XY universality class. For this universality class one has $\nu z \simeq 0.67$ [42, 45]. Converted to our units, the critical point lies at $h_c = 0.303(9)$ [46]. Our results are listed in Table 4.5. 4.5a shows the extrapolation results for the critical field strength $-h_c$. Although our results fluctuate, this is mirrored by the big uncertainty. Powalski at al. [47] used the same series expansion and extrapolation methods and investigated this transverse field Ising model up to 13th order, where they found the second-order phase transition at $h_c = 0.305$. The results for the critical exponent, listed in Table 4.5b, vary strongly. Here the DLogPadé approximations for $[L, M] = [2, 4]$ and $[3, 3]$ seem to be the most accurate, considering the already mentioned overestimation of νz. At this point it should be noted, that the polarized high-field phase is not located in the charge-free sector. This means, that we expect a first-order phase transition phase between a charge-free and a polarized phase for $h_x < 0$ beyond the topological phase.

$L\backslash M$	1	2	3	4	5
1	0.107527	0.105477	0.105238	0.105092	0.105047
2	0.104729	0.105231	0.104545	0.105036	–
3	0.105341	0.105097	0.105032	–	–
4	0.104936	0.105044	–	–	–
5	0.105082	–	–	–	–

(a)

$L\backslash M$	1	2	3	4	5
1	0.693722	0.658215	0.652980	0.648983	0.647482
2	0.640980	0.652782	0.620996	0.647027	–
3	0.656081	0.649125	0.646876	–	–
4	0.643577	0.647364	–	–	–
5	0.648979	–	–	–	–

(b)

Table 4.4: Results from the DLogPadé$[L, M]$ extrapolations for the single parallel field h_x with $h_x > 0$. (a) Results for the critical field strength h_c. (b) Results for the critical exponent νz.

$L\backslash M$	1	2	3	4	5
1	–	0.333333	0.303126	0.310052	0.302332
2	–	0.295630	0.308637	0.306201	–
3	–	–	0.315060	–	–
4	–	0.296605	–	–	–
5	–	–	–	–	–

(a)

$L\backslash M$	1	2	3	4	5
1	–	0.888888	0.705399	0.759727	0.683736
2	–	0.647626	0.745474	0.724830	–
3	–	–	0.716233	–	–
4	–	0.617616	–	–	–
5	–	–	–	–	–

(b)

Table 4.5: Results from the DLogPadé$[L, M]$ extrapolations for the single parallel field h_x with $h_x < 0$. (a) Results for the critical field strength $-h_c$. (b) Results for the critical exponent νz. Values marked with an asterisk denote defective extrapolations. Note, that the results for the DLogPadé$[L, 1]$ and DLogPadé$[3, 2]$ extrapolations are not depicted, since non-physical poles distorted the results significantly.

4.3.3 Parallel fields

After comparing our results for the Ising line, the next step is to investigate the critical behaviour for a parallel field. For this, we will represent the field again as a vector $\mathbf{h} = (h_x, h_y, h_z)$. For the parallel case, we have $h_y = 0$, thus $\mathbf{h} = h(\cos(\phi), 0, \sin(\phi))$. The Ising lines can be obtained by choosing $\phi = 0$, $\frac{\pi}{2}$ or π. Since this system is only symmetric in h_z, critical field strengths and exponents have to be calculated for $\phi \in [0, \pi]$. With this, one has to extrapolate Δ_c and $\Delta_{f,h_x^\pm}$ for every ϕ and check, which particle condenses first. The resulting critical points h_c are depicted in Figure 4.11. In the domain marked by (I), the flux condenses first. In the area labeled by (II), the charge condenses first. Both of these domains exhibit critical behaviour in the 3D-Ising universality class. Only in domain (III), the critical points belong to a phase transition inside the 3D-XY universality class. In this domain the fluxes condense first for $h_x < 0$.
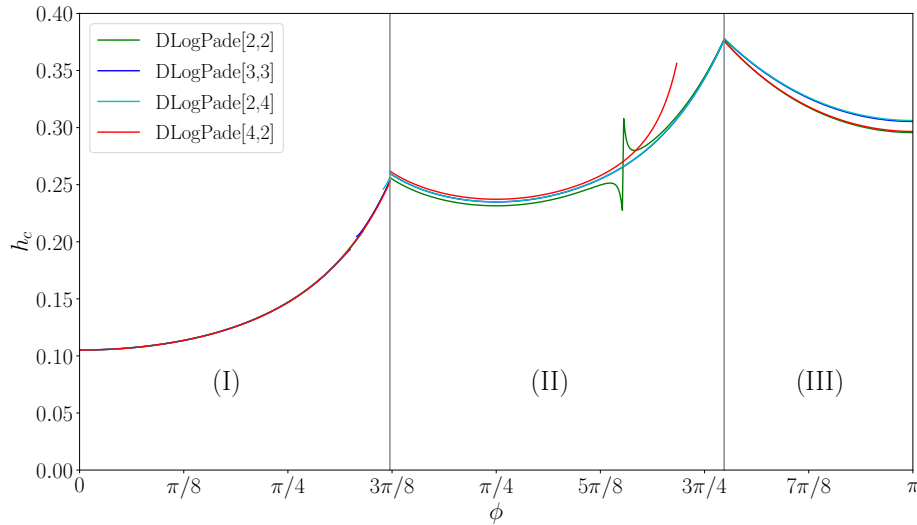

Figure 4.11: Approximants for the critical field strength h_c for increasing ϕ. The vertical grey lines mark the domain walls or multicritical points. In domain (I) and (III), the flux condenses first, while in (II), the charge condenses first. The domain walls lie at $\phi_{c_1} = 1.17$ and $\phi_{c_2} = 2.43$.

The critical exponent νz for these three domains is depicted in Figure 4.12. One can see, that in the domains (I) and (II) the critical exponent stays almost constantly at $\nu z \simeq 0.65$. The small deviations near the domain wall between (I) and (II) are non-physical poles. νz takes a slightly higher value at the multicritical point $\phi_{c_1} = 1.17$ in domain (II), although this increase is to small to indicate a different universality class. This means, that for the honeycomb lattice our results for the critical exponent at the multicritical point, where charges and fluxed condense simultaneously, do not mirror the rising critical exponent at the multicritical point for the square lattice, as discussed
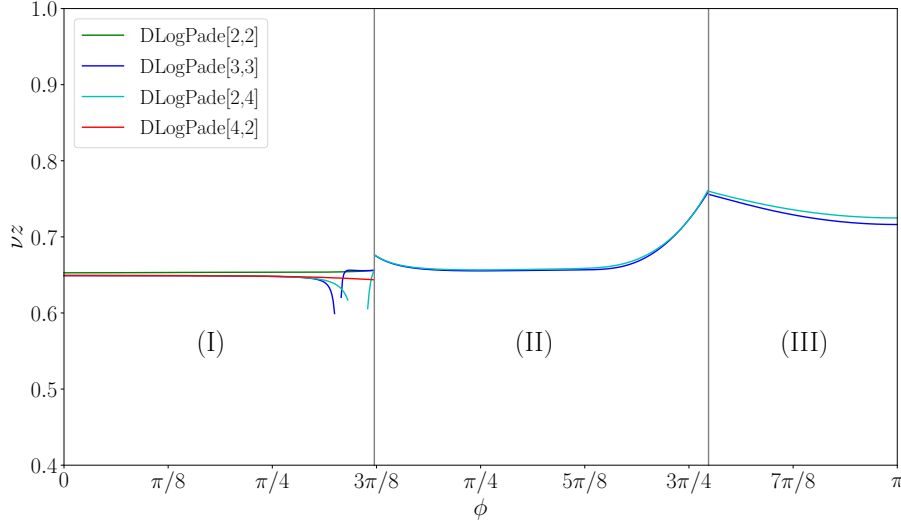
47

Figure 4.12: Critical exponent νz along the phase transition, parameterized by ϕ. The labels (I) to (III) denote the same domains as in Figure 4.11. In the domains (I) and (II) and at their domain wall or multicritical point $\phi = 1.17$ the critical exponent remains almost constant at $\nu z \simeq 0.65$, with the exception of deviations, which could be attributed to non-physical poles. Only near the multicritical point between domains (II) and (III) with $\phi = 2.43$, the critical exponent grows significantly to $\nu z \simeq 0.77$. In domain (III), the critical exponent falls again to $\nu z \simeq 0.71$

in subsection 4.2.3. In domain (II), near the second multicritical point $\phi_{c2} = 2.43$, the critical exponent increases significantly to $\nu z \simeq 0.77$. While this could indicate a 3D-XY universality class, the exponent falls notably in domain (III). This suggests, that at this multicritical point a different universality class is realized. To confirm this, extrapolations of higher orders, especially in domain (III) are needed, to further investigate the precise course of νz.

Figure 4.11 can also be reconstructed, to display a phase diagram of the toric code in a parallel field on a honeycomb lattice. This phase diagram is depicted in Figure 4.13. While now, the phase transitions out of the topological phase are known, properties of the phases, which lie outside the marked area, have yet to be investigated.
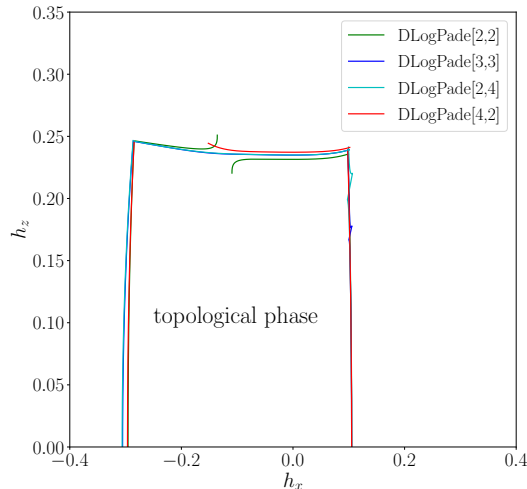
Figure 4.13: Quantum phase diagram of the toric code on a honeycomb lattice in a parallel field. The topological phase is separated by a second-order phase transition, indicated by lines, from other phases outside the marked area.

4.3.4   Parallel and transverse field

After investigating the case, in which the present fields are parallel, we will consider the parallel and transverse field together. Unlike in the previous section, where first-order phase transitions have already been found [21], we do not have any results for the toric code on the honeycomb lattice. Here, we will only calculate second-order phase transitions. For this, we again consider the field-vector $\mathbf{h} = (h_x, h_y, h_z) = h(\sin(\phi)\cos(\theta), \sin(\theta), \cos(\phi)\cos(\theta))$. For $\theta = 0$, we recover the parallel field case. To analyze the topological phase for a transverse field, the angle θ is increased form $\theta = 0$ to $\theta = \frac{\pi}{2}$. For θ near $\frac{\pi}{2}$ a first-order phase transition was found for the square lattice [21], such that a critical θ_c was calculated, at which the system entered a domain, in which phase transitions were no longer continuous. In our case, we will present the approximants for the critical points for increasing θ, until the DLogPadé approximations no longer converge. Here it is important to note, that other phase transitions, namely first-order ones can occur, which cannot be detected with our methods.

We will now consider different cases. First we investigate the behaviour of the Ising lines, discussed in subsection 4.3.2. There one has $\phi = 0$, $\frac{\pi}{2}$ and π. From there, θ is increased. The critical field strengths and the corresponding critical exponents are depicted in Figure 4.14. One can see, that for all cases, the critical point only increases minimally, while the critical exponent stays constant at $\nu z = 0.65$ for $\phi = 0$ and increases for $\phi = \frac{\pi}{2}$ form $\nu z = 0.65$ to $\nu z \simeq 0.75$. For $\phi = \pi$, the extrapolations for the critical exponent exhibit poles around the cutoff-angle, that mirror poles for the critical field strength. Nonetheless, after the pole the approximants return to their

49

almost constant value of $\nu z = 0.71$. This leads us to the assumption, that along these lines the universality classes do not change. The extrapolation for the behaviour of the Ising lines is relatively stable for large θ, which is no longer the case for the behaviour of the multicritical points, which are discussed next.

Here, the analysis of the multicritical lines, meaning multicritical points for increasing transversal field strength, is more complicated than for the square lattice, since the multicritical lines are no longer found at a constant angle ϕ. Although ϕ only changes by small amount, this has to be take into consideration, while calculating the course of the multicritical lines. This has been done, by increasing θ step-wise, and adjusting the multicritical angle ϕ_c. Additionally, both multicritical lines represent domain boundaries between two domains, visualized in Figure 4.11, on which approximants from two domains have to be calculated on a boundary. The critical points and exponents along the multicritical lines are depicted in Figure 4.15. There, for the multicritical line, that separates the domains (I) and (II), approximants out of each domain have been depicted. The same holds for the boundary between (II) and (III). The multicritical point is defined by the fact that the critical values in two different domains take the same value at said point. This is the case for both lines 4.15 (a) and (c). Here one also can see that near the cutoff-angle the approximants diverge.

Let us now inspect the critical values along the multicritical lines. In 4.15 (b), the critical exponent of both domains (I) and (II), which both exhibit a phase transition belonging to the 3D-Ising universality class, is converged towards a value of $\nu z \simeq 0.67$ for $\theta < \frac{\pi}{8}$. For $\theta > \frac{\pi}{8}$, the approximants for the two domains diverge, until they converge again at $\phi \simeq \frac{7\pi}{32}$. The divergence might be due to extrapolation errors. To gain certainty, higher orders have to be calculated. Still, the notable increase in νz indicates a change in universality class, provided, no first-order phase transition is present before this increase. A different case presents itself for the domain wall between domains (II) and (III). These domains exhibit phase transitions that belong to different universality classes, namely 3D-Ising and 3D-XY, respectively. In Figure 4.15 (d), the critical exponent, which belongs to domain (II), diverges quickly, while the critical exponent belonging to domain (III) stays almost constant. Due to the unconventional behaviour of νz in domain (II) for a increasing transverse field, we cannot make a conclusion about the universality class along this multicritical line. A possible explanation for this behaviour could be, that, unlike for the square lattice, the gaps Δ_{f,h_x^-} and Δ_c have different momenta, as mentioned in subsection 4.3.1.

Finally, from these results, a sketch of the phase-diagram for a three-dimensional field is presented in Figure 4.16. On the $h_x - h_z$ plane, for $h_y = 0$, one can recognize the phase diagram presented in Figure 4.13. For $h_y > 0$, the multicritical lines and the Ising lines for $h_z = 0$ are sketched. The surfaces marked by (I) and (II) correspond to domains (I) and (II), where the phase transitions is of the 3D-Ising universality class. The surface marked by (III) represents domain (III), where the phase transition was found to be in the 3D-XY universality class. Here, it should be stressed again, that we do not have any insight into additional, first-order phase transitions that could occur for $h_y > 0$.
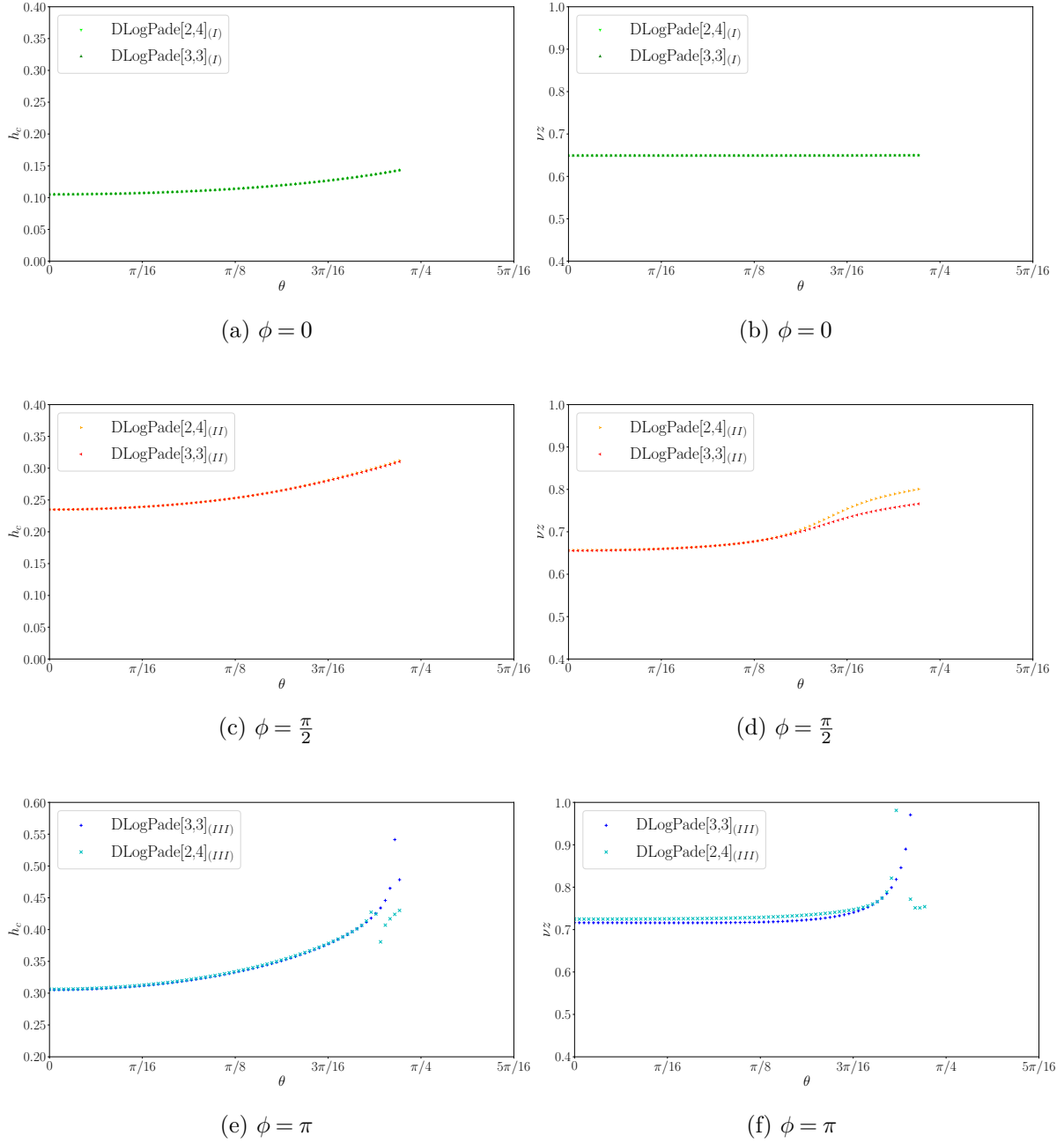
Figure 4.14: Critical points and exponents for the Ising lines for increasing θ. (a) and (b) show the critical behaviour for $\phi = 0$, (c) and (d) for $\phi = \frac{\pi}{2}$ and (e) and (f) for $\phi = \pi$. The indices (I) to (III) denote, in which domain, discussed in subsection 4.3.3, the Ising line lies. Values are plotted up to the cutoff-angle of $\theta_0 = 0.75$
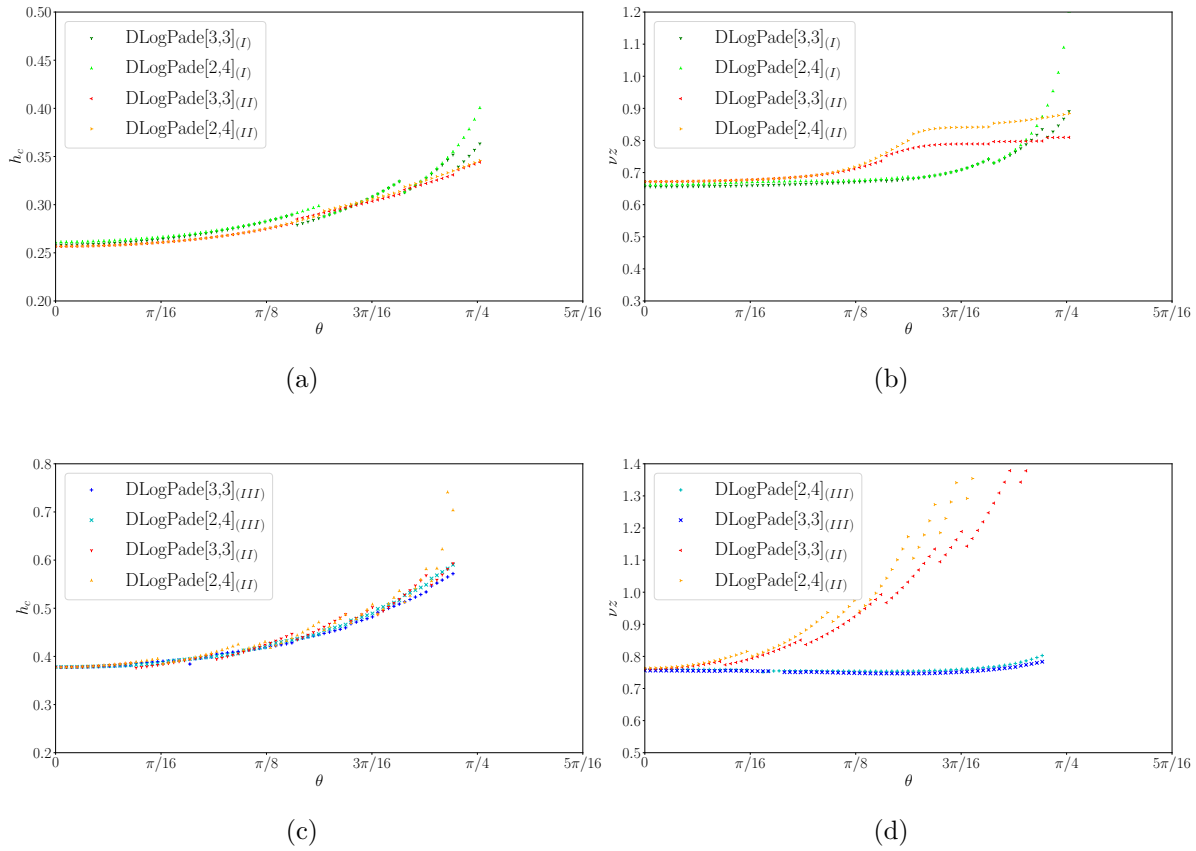
Figure 4.15: Critical points and exponents for the multicritical lines, parameterized by θ. (a) and (b) show the critical behaviour for the boundary between domains (I) and (II), (c) and (d) the boundary between (II) and (III). The indices (I) to (III) denote, the approximants out of different domains. At $\theta_0 = 0.75$ the DLogPadé approximants begin to diverge. Updating the angle ϕ_c of the multicritical point in discrete values results in step-function-like behaviour for some approximants.
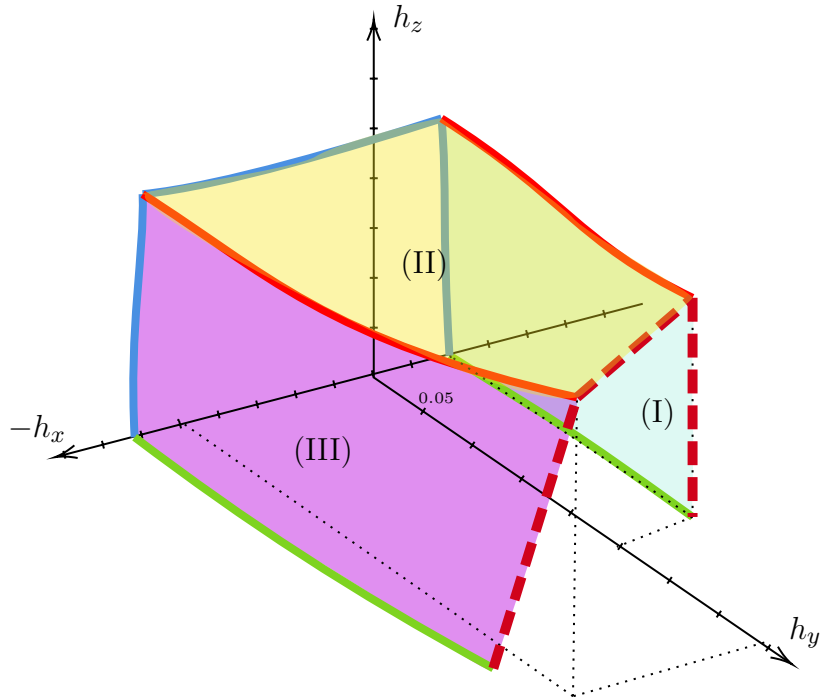
Figure 4.16: Sketch of the quantum phase diagram of the toric code on a honeycomb lattice in a uniform magnetic field. The topologically-ordered phase is enclosed by the surfaces (I), (II) and (III), which represent second-order phase transitions and correspond to the different domains. Green lines depict the development of the Ising lines for $h_z = 0$. Blue lines show the phase diagram for a parallel field, as shown in subsection 4.3.3. Red, continuous lines outline the multicritical lines. The dashed, red lines indicate the end of the validity of our approximations.

5. Conclusions

In this thesis we used linked-cluster expansion, to investigate the toric code in a magnetic field at zero temperature. First this was done on a square lattice, where results were already known [21], then on a honeycomb lattice, which was not thoroughly studied yet. We used mappings onto different lattices, full graph decomposition of the underlying lattices and perturbative continuous unitary transformations, to calculate the dispersions and mass gaps of the single particles, that exist on the toric code. The perturbative series, that was gained using the pCUT method, was then approximated by using Padé and dLogPadé extrapolations. With these, the critical points and exponents were calculated, such that phase diagrams for different field directions could be drawn.

For the toric code on the square lattice, we were able to surpass the perturbation order in [21] by one, while using less computation time. We found the second-order phase transitions, which belong to the 3D-Ising universality class. With the higher perturbation order, it was possible to confirm the results and support the conjectures about a different universality class on the multicritical point ($h_x = h_z$, $h_y = 0$) and on the multicritical line ($h_x = h_z$, $h_y \neq 0$), which were made in [21]. Nonetheless, we did not gain further insight into the exact moment, in which the universality class changes on the multicritical line. For the multicritical point and line, the change of critical behaviour could be attributed to the simultaneous condensation of charges and fluxes, which have exotic mutual exchange statistics. However, unlike done in [21], we were not able to locate first-order phase transitions with our method.

For the toric code on the honeycomb lattice, which was not yet an object of much research, we also calculated relevant particle dispersions and mass gaps for different field configurations. The perturbation order achieved was 7. Here we again used the same methods as for the square lattice and were able to detect different phase transitions. An important difference to the toric code on the square lattice is, that for the case on the honeycomb lattice, self-duality and certain symmetries are not present. This stems from the fact, that the dual models realize geometric frustration for certain cases. Hence, for the toric code on the honeycomb lattice, not only phase transitions belonging to the 3D-universality class have been found, like it is the case for our calculations on the square lattice, but also ones that belong to the 3D-XY universality class. This 3D-XY phase transition could be traced back to the mapping of the model onto an antiferromagnetic transverse-field Ising model on a triangular lattice. We were able to calculate a phase diagram for an arbitrary field direction. Here we also investigate

the multicritical lines, where, in some cases, we could not make any statements about universality classes, due to diverging behaviour of different approximations. At this point, it has to be stressed again, that we were not able to find any phase transition for large h_y. One would, analogously to the model on a square lattice, expect first-order phase transitions. To find those, one could use projected entangled pair states, as done in [21] for the square lattice, variational studies or a high-field series expansion. These transitions, depending on where they would lie, would invalidate at least some of our results presented in this thesis. To do this, further studies are needed.

Bibliography

[1] X. G. Wen. "Vacuum degeneracy of chiral spin states in compactified space". In: *Phys. Rev. B* 40 (10 1989), pp. 7387–7390.

[2] X. G. Wen, Frank Wilczek, and A. Zee. "Chiral spin states and superconductivity". In: *Phys. Rev. B* 39 (16 1989), pp. 11413–11423.

[3] X. G. Wen and Q. Niu. "Ground-state degeneracy of the fractional quantum Hall states in the presence of a random potential and on high-genus Riemann surfaces". In: *Phys. Rev. B* 41 (13 1990), pp. 9377–9396.

[4] Sergey Bravyi, Bernhard Leemhuis, and Barbara M. Terhal. "Topological order in an exactly solvable 3D spin model". In: *Annals of Physics* 326.4 (2011), pp. 839–866.

[5] A.Yu. Kitaev. "Fault-tolerant quantum computation by anyons". In: *Annals of Physics* 303.10 (2003), pp. 2–30.

[6] Michael A. Levin and Xiao-Gang Wen. "String-net condensation: A physical mechanism for topological phases". In: *Phys. Rev. B* 71 (4 2005), p. 045110.

[7] H. Bombin and M. A. Martin-Delgado. "Topological Quantum Distillation". In: *Phys. Rev. Lett.* 97 (18 2006), p. 180501.

[8] Alexei Kitaev. "Anyons in an exactly solved model and beyond". In: *Annals of Physics* 321.1 (2006), pp. 2–111.

[9] R. Moessner and S. L. Sondhi. "Resonating Valence Bond Phase in the Triangular Lattice Quantum Dimer Model". In: *Phys. Rev. Lett.* 86 (9 2001), pp. 1881–1884.

[10] A. Ioselevich, D. A. Ivanov, and M. V. Feigelman. "Ground-state properties of the Rokhsar-Kivelson dimer model on the triangular lattice". In: *Phys. Rev. B* 66 (17 2002), p. 174405.

[11] K. J. Satzinger et al. "Realizing topologically ordered states on a quantum processor". In: *Science* 374.6572 (2021), pp. 1237–1241.

[12] J K Pachos et al. "Revealing anyonic features in a toric code quantum simulation". In: *New Journal of Physics* 11.8 (2009), p. 083010.

[13] Sergey Bravyi and Matthew B. Hastings. "A Short Proof of Stability of Topological Order under Local Perturbations". In: *Communications in Mathematical Physics* 307.3 (2011), pp. 609–627.

[14] Claudio Castelnovo and Claudio Chamon. "Entanglement and topological entropy of the toric code at finite temperature". In: *Physical Review B* 76.18 (2007).

[15] Simon Trebst et al. "Breakdown of a Topological Phase: Quantum Phase Transition in a Loop Gas Model with Tension". In: *Phys. Rev. Lett.* 98 (7 2007), p. 070602.

[16] Damian Abasto, Alioscia Hamma, and Paolo Zanardi. "Fidelity analysis of topological quantum phase transitions". In: *Physical Review A* 78 (Apr. 2008).

[17] Julien Vidal et al. "Self-duality and bound states of the toric code model in a transverse field". In: *Phys. Rev. B* 80 (8 2009), p. 081104.

[18] Julien Vidal, Sébastien Dusuel and Kai Phillip Schmidt. "Low-energy effective theory of the toric code model in a parallel field". In: *PHYSICAL REVIEW B* 79.033109 (2009).

[19] Fengcheng Wu, Youjin Deng and Nikolay Prokof'ev. "Phase diagram of the toric code model in a parallel magnetic field". In: *PHYSICAL REVIEW B* 85.195104 (2012).

[20] I. S. Tupitsyn et al. "Topological multicritical point in the phase diagram of the toric code model and three-dimensional lattice gauge Higgs model". In: *Phys. Rev. B* 82 (8 2010), p. 085114.

[21] Sébastien Dusuel et al. "Robustness of a Perturbed Topological Phase". In: *Phys. Rev. Lett.* 106 (10 2011), p. 107203.

[22] Alastair Kay. "Nonequilibrium Reliability of Quantum Memories". In: *Phys. Rev. Lett.* 102 (7 2009), p. 070503.

[23] Kai Phillip Schmidt. "Persisting topological order via geometric frustration". In: *Phys. Rev. B* 88 (3 2013), p. 035118.

[24] Sébastien Dusuel et al. "Bound states in two-dimensional spin systems near the Ising limit: A quantum finite-lattice study". In: *Phys. Rev. B* 81 (6 2010), p. 064412.

[25] Michael Kamfor. "Robustness and spectroscopy of the toric code in a magnetic field". PhD thesis. Technische Universität Dortmund Université Pierre-et-Marie-Curie, 2013.

[26] Knetter, C. and Uhrig, G. S. "Perturbation theory by flow equations: dimerized and frustrated S=1/2 chain". In: *Eur. Phys. J. B* 13.2 (2000), pp. 209–225.

[27] Christian Knetter, Kai P Schmidt, and Götz S. Uhrig. "The structure of operators in effective particle-conserving models". In: *Journal of Physics A: Mathematical and General* 36.29 (2003), pp. 7889–7907.

[28] Jaan Oitmaa, Christopher Hamer, and Weihong Zheng. "Series Expansion Methods for Strongly Interacting Lattice Models". In: *Series Expansion Methods for Strongly Interacting Lattice Models* (Jan. 2006).

[29] Martin P. Gelfand and Rajiv R. P. Singh. "High-order convergent expansions for quantum many particle systems". In: *Advances in Physics* 49.1 (2000), pp. 93–140.

[30] David A. Reiss and Kai Phillip Schmidt. "Quantum robustness and phase transitions of the 3D Toric Code in a field". In: *SciPost Phys.* 6 (2019), p. 078.

[31] Zohar Nussinov and Gerardo Ortiz. "A symmetry principle for topological quantum order". In: *Annals of Physics* 324.5 (2009), pp. 977–1057.

[32] Zohar Nussinov and Gerardo Ortiz. "Sufficient symmetry conditions for Topological Quantum Order". In: *Proceedings of the National Academy of Sciences* 106.40 (2009), pp. 16944–16949.

[33] Henk W. J. Blöte and Youjin Deng. "Cluster Monte Carlo simulation of the transverse Ising model". In: *Phys. Rev. E* 66 (6 2002), p. 066110.

[34] S. V. Isakov and R. Moessner. "Interplay of quantum and thermal fluctuations in a frustrated magnet". In: *Phys. Rev. B* 68 (10 2003), p. 104409.

[35] Franz J. Wegner. "Flow equations for Hamiltonians". In: *Physics Reports* 348.1 (2001). Renormalization group theory in the new millennium. II, pp. 77–89. ISSN: 0370-1573.

[36] Stanisław D. Głazek and Kenneth G. Wilson. "Renormalization of Hamiltonians". In: *Phys. Rev. D* 48 (12 1993), pp. 5863–5872.

[37] K. Coester and K. P. Schmidt. "Optimizing linked-cluster expansions by white graphs". In: *Physical Review E* 92.2 (2015).

[38] Kris Coester et al. "Linked-cluster expansions for quantum magnets on the hypercubic lattice". In: *Phys. Rev. B* 94 (12 2016), p. 125109.

[39] S. Sachdev. *Quantum phase transitions.* Cambridge University Press.

[40] A. J. Guttmann. *Asymptotic analysis of power-series expansions.* In Phase Transitions and Critical Phenomena, Volume 13. Edited by C. Domb and J. L. Lebowitz. 1989.

[41] S. V. Isakov et al. "Dynamics at and near conformal quantum critical points". In: *Phys. Rev. B* 83 (12 2011), p. 125114.

[42] A. Pelissetto and E. Vicari. "Critical phenomena and renormalization-group theory". In: *Physics Reports* 368.6 (2002), pp. 549–727. ISSN: 0370-1573.

[43] Sebastian Fey. "Investigation of zero-temperature transverse-field Ising models with long range interactions". PhD thesis. Germany: Friedrich–Alexander University Erlangen–Nürnberg, 2020.

[44] Philippe Corboz et al. "Simulation of strongly correlated fermions in two spatial dimensions with fermionic projected entangled-pair states". In: *Phys. Rev. B* 81 (16 2010), p. 165104.

[45] A. P. Gottlob and M. Hasenbusch. "The XY model and the three-state antiferromagnetic Potts model in three dimensions: Critical properties from fluctuating boundary conditions". In: *Journal of Statistical Physics* 77 (3 1994), pp. 919–930.

[46] S. V. Isakov and R. Moessner. "Interplay of quantum and thermal fluctuations in a frustrated magnet". In: *Phys. Rev. B* 68 (10 2003), p. 104409.

[47]   M. Powalski et al. "Disorder by disorder and flat bands in the Kagome transverse field Ising model". In: *Phys. Rev. B* 87 (5 2013), p. 054404.

Acknowledgements

First of all, I would like to thank my supervisor Prof. Dr. Kai Philipp Schmidt for giving me the opportunity to write this thesis. I am very thankful for his patience, time and guidance throughout the last year. Matthias Wühlmauser deserves special thanks for not only letting me use is code, but also the many hours in which he explained it to me and for proofreading this thesis. Additionally i want to thank Matthias Walther and Andreas Schellenberger for also proofreading this thesis. I further want to thank everyone mentioned above, Lea Lenke and Raymond Wiedmann for many fruitful discussions.

Overall, I also thank the whole Theorie-I group for the pleasant and fun times during the last year.

Finally I would like to thank my family, especially my dog, for their constant support during my studies.

Eigenständigkeitserklärung

Hiermit versichere ich, dass ich die vorliegende Arbeit selbstständig verfasst habe, keine anderen als die angegebenen Quellen benutzt habe, dass alle Stellen der Arbeit, die wörtlich oder sinngemäß aus anderen Quellen übernommen wurden, als solche kenntlich gemacht worden sind und dass die Arbeit in gleicher oder ähnlicher Form noch keiner Prüfungsbehörde vorgelegt wurde.

Erlangen, den 31. Oktober 2022

Viktor Kott